

NASA TECHNICAL NOTE



NASA TN D-5553

2.1

NASA TN D-5553



LOAN COPY: RETURN TO
AFWL (WL0L)
KIRTLAND AFB, N MEX

EXPERIMENTAL DETERMINATION
OF EQUIVALENT SOLID BODIES
TO REPRESENT JETS EXHAUSTING
INTO A MACH 2.20 EXTERNAL STREAM

by Lawrence E. Putnam and Francis J. Capone

Langley Research Center

Langley Station, Hampton, Va.



0132604

1. Report No. NASA TN D-5553	2. Government Accession No.	3. Recipient's Catalog No.
4. Title and Subtitle EXPERIMENTAL DETERMINATION OF EQUIVALENT SOLID BODIES TO REPRESENT JETS EXHAUSTING INTO A MACH 2.20 EXTERNAL STREAM		5. Report Date December 1969
7. Author(s) Lawrence E. Putnam and Francis J. Capone		6. Performing Organization Code
9. Performing Organization Name and Address NASA Langley Research Center Hampton, Va. 23365		8. Performing Organization Report No. L-6707
12. Sponsoring Agency Name and Address National Aeronautics and Space Administration Washington, D.C. 20546		10. Work Unit No. 720-03-11-01-23
15. Supplementary Notes		11. Contract or Grant No.
16. Abstract <p>An inverse application of the method of characteristics for potential axially symmetric flow has been developed to calculate an equivalent solid body which will produce the same interference pressure field as an axially symmetric jet exhausting into a supersonic stream. An experimental investigation has also been made at a Mach number of 2.20 to obtain measurements of local Mach number, flow angle, and pressure in the flow field of cold air jets exhausting from various axially symmetric nozzle configurations. These flow-field measurements were used in calculations of equivalent solid bodies to represent jet exhaust plumes for various nozzle operating conditions.</p> <p>A comparison of the flow fields produced by two jet equivalent solid bodies and flow fields of the corresponding jet plumes showed good agreement and verified the present concept of representing a jet plume by an equivalent solid body.</p>	13. Type of Report and Period Covered Technical Note	
17. Key Words Suggested by Author(s) Jet plumes Supersonic flow Jet interference	18. Distribution Statement Unclassified - Unlimited	14. Sponsoring Agency Code
19. Security Classif. (of this report) Unclassified	20. Security Classif. (of this page) Unclassified	21. No. of Pages 66
		22. Price* \$3.00

*For sale by the Clearinghouse for Federal Scientific and Technical Information
Springfield, Virginia 22151

EXPERIMENTAL DETERMINATION OF EQUIVALENT
SOLID BODIES TO REPRESENT JETS EXHAUSTING INTO A
MACH 2.20 EXTERNAL STREAM

By Lawrence E. Putnam and Francis J. Capone
Langley Research Center

SUMMARY

An inverse application of the method of characteristics for potential axially symmetric flow has been developed to calculate an equivalent solid body which will produce the same interference pressure field as an axially symmetric jet exhausting into a supersonic stream. The effects on sonic-boom pressure signatures of supersonic airplanes can be determined with present analytical methods by representing jet exhaust plumes with the corresponding jet equivalent solid body. The jet-plume interference effects on adjacent airframe surfaces can also be determined provided adequate near field methods of calculating induced flow fields become available.

An experimental investigation has been made at a free-stream Mach number of 2.20 to obtain measurements of local Mach number, flow angle, and pressure in the flow field of cold air jets exhausting from various axially symmetric nozzle configurations. Flow-field measurements were also made for the jet-engine nacelle simulator (a 14° cone-cylinder body) and for two jet equivalent solid bodies calculated from the jet-plume flow-field data. A comparison of the calculated body shape corrected for boundary-layer displacement thickness indicated excellent agreement with the actual body geometry of the engine simulator. The good agreement between the flow-field signatures produced by the two jet equivalent solid bodies and the corresponding jet plumes has verified the present concept of representing a jet plume by an equivalent solid body.

Comparisons have shown that the calculated radius of the theoretical inviscid jet boundaries for all nozzles and jet pressure ratios of the present tests increase considerably faster with longitudinal distance downstream of the nozzle exit than the corresponding jet equivalent solid bodies. Calculations have also shown considerable effects of the jet plumes on the trailing-shock-wave system in the near field sonic-boom signatures of two representative supersonic airplanes with podded engines.

INTRODUCTION

Current analytical methods of evaluating the supersonic wave (pressure) drag of airplanes (ref. 1) and the sonic-boom overpressure (refs. 2 and 3) depend for their accuracy on a detailed knowledge of the effective shape of the airplane. These theoretical methods, at present, represent the engine exhaust jet analytically by a cylindrical stream tube extending to infinity downstream from the exhaust-nozzle exit. However, since the pressure of the exhaust gases at the nozzle exit is generally different from ambient pressure, the jet will tend either to plume or to contract on leaving the nozzle. Furthermore the shape of the jet plume downstream of the nozzle exit will be affected by the viscous mixing between the jet exhaust and the external stream. In principle these deviations of the jet exhaust from a cylindrical stream tube can result in aerodynamic interference on adjacent airframe surfaces.

The present investigation was undertaken to find the shape of equivalent solid bodies which would produce the same interference flow field as a propulsive jet. These equivalent solid bodies will have application in calculations of the interference effects of propulsive jets on the external pressure drag, the lift, and the sonic-boom pressure signatures of supersonic airplanes; for example, this can be accomplished in the case of sonic-boom pressure signatures by incorporating the equivalent solid body in the geometry of a supersonic airplane to represent the jet plume.

The inviscid boundary between a jet plume and the external stream can be calculated by various means such as the method of reference 4, the method of characteristics, or any of several simplified procedures based on the method of characteristics. (See, for example, refs. 5 and 6.) However, as a result of viscous effects such as the mixing between the jet plume and the external stream and the boundary layer on the exhaust nozzle, the inviscid jet boundary will probably differ from both the actual boundary and the equivalent solid body representation of the jet plume. (See refs. 7 and 8.) In the present paper an inverse axially symmetric method of characteristics solution (that is, boundary calculated from a specified flow field rather than the flow field calculated from a specified boundary) has been developed to calculate the jet equivalent solid body from flow-field signatures consisting of measurements of local Mach number and flow angle in the external flow field surrounding the jet plume. A description and a discussion of the procedure are given in appendixes A and B.

Experimental measurements were made in the Langley 4- by 4-foot supersonic pressure tunnel at a free-stream Mach number of 2.20 to provide Mach number and flow-angle signatures for jets exhausting into a supersonic stream from which equivalent solid bodies were calculated. The experimental investigation was conducted in two phases. During phase I flow-field signatures were obtained for one nozzle configuration (configuration 4

herein) on an air-powered jet-engine exhaust-nozzle simulator with the jet off and with the jet operating at the ratio of jet static pressure to free-stream static pressure of 1.093. These flow-field signatures were then used to calculate the corresponding equivalent solid bodies. Phase II of the investigation was conducted to verify the analytical procedure used to calculate the equivalent solid bodies. During this phase of the investigation, flow-field signatures were obtained for the equivalent solid bodies to compare with the interference signatures obtained for the corresponding jet plume. During phase II, flow-field signatures were measured for several additional nozzle configurations at various operating conditions.

SYMBOLS

A	area
C_L	lift coefficient based on wing planform area
d	diameter
D	maximum diameter of simulator (15.24 centimeters)
k	boattail surface length
L	overall model length
M	Mach number
p	pressure
p_t	stagnation pressure
$\Delta p = p_t - p_\infty$	
r	radial coordinate
r_0	radius at start of jet equivalent solid body
R	Reynolds number based on D
s	longitudinal distance from nozzle throat to nozzle exit

T_t	stagnation temperature
V	local velocity
W	ratio of local velocity to limiting velocity
x	longitudinal coordinate
y	radial distance from model surface
z	radial location of survey line
α	nozzle-divergence angle
β	boattail angle
δ^*	boundary-layer displacement thickness
θ	flow angle
μ	Mach angle, $\sin^{-1} \frac{1}{M}$
ϕ	roll angle; meridian angle
ψ	shock angle

Subscripts:

A,B,C,D,E	conditions at points A, B, C, D, and E, respectively
b	base
des	design
e	exit
i	impact
j	jet; conditions at nozzle exit

l	local
n	nozzle
th	throat
∞	free stream

APPARATUS

Exhaust-Nozzle Simulation System

A sketch of the strut-supported jet-engine exhaust-nozzle simulation system used in the present investigation is presented as figure 1. The nacelle consisted of a conical forebody with half-angle of 14° , a cylindrical centerbody of 15.24-centimeter diameter, and various interchangeable afterbody nozzle configurations. The nacelle was strut-supported from the tunnel side wall, and the strut had a leading-edge sweep of 45° and a 5-percent-thick (streamwise) hexagonal airfoil. High-pressure heated air (line pressure 5000 kilonewtons/meter²) is brought through the strut in six air lines into an annular chamber and is then discharged into the nozzle through a series of eight small (0.95-centimeter) circumferential nozzles. (See fig. 1.) Maximum stagnation pressure in the nozzle settling chamber is approximately 690 kN/m² and the nozzle stagnation temperature is approximately 300° K.

This simulation system was designed to study both internal and external nozzle performance and hence utilizes extensive instrumentation such as a strain-gage force balance to measure nozzle thrust minus drag, flow meters, thermocouples, and pressure gages. However, for the present investigation, only the instrumentation necessary to measure the quantities pertinent to the basic objective of the tests were utilized.

In addition to the afterbody nozzle configurations, two cylindrical afterbody configurations with blunt bases could be attached to the jet-engine exhaust-nozzle simulator. These cylindrical afterbodies have several longitudinal rows of static-pressure orifices located at various meridian angles so that interference effects of the support strut could be determined. The overall lengths of 113.28 centimeters and 119.38 centimeters for the simulator with the cylindrical afterbodies essentially bracket the location of the exit of the various nozzle configurations. Provision was also made for three boundary-layer rakes to be located 45° apart at two longitudinal positions on the cylindrical afterbodies. The rakes could be rolled 90° so that 180° of the afterbody could be surveyed. (See fig. 1.) In addition a cone-cylinder body identical to the simulator, except sting mounted, was available for testing. This model was 119.38 centimeters long and the sting diameter

was 3.81 centimeters. A single row of static-pressure orifices was located along the length of this body.

Nozzle and Equivalent Solid Bodies

The geometrical characteristics of the seven nozzles used in the present investigation are presented as figure 2. The nozzles were of the convergent-divergent type with five of the nozzles having boattails of 0° . Each nozzle had a stagnation temperature and pressure probe located in the nozzle settling chamber. In addition static-pressure orifices were located on the nozzle wall. A nozzle-wall static-pressure orifice located approximately 0.76 centimeter from the nozzle exits was used to determine nozzle-exit static pressure.

Coordinates for the two equivalent solid bodies are presented in table I. (A discussion of the procedure used to calculate these equivalent solid bodies is presented subsequently herein.) These two solid bodies were extended downstream approximately 0.5 model maximum diameter with the same slope as the last equivalent body point where ordinates were computed from flow-field surveys so as to reduce interference caused by the proximity of the flow expanding into the blunt base region.

Probe and Survey Apparatus

The wind-tunnel-apparatus arrangement used to survey the flow fields is shown in figure 3. The measuring probe was mounted on a support system which provided remote control of the longitudinal and lateral position. Vertical position of the probe could be changed manually.

A sketch of the probe used for the flow-field studies is shown in figure 4. This probe had a 15° half-angle cone with four 0.05-centimeter-diameter static-pressure orifices located circumferentially 90° apart on the cone and a 0.05-centimeter-diameter stagnation-pressure orifice located at the tip of the probe.

Wind Tunnel and Instrumentation

The investigation was conducted in the Langley 4- by 4-foot supersonic pressure tunnel. Tests can be made in the continuous flow tunnel at stagnation pressures from approximately 28 kN/m² to 207 kN/m² at a stagnation temperature of 316.67° K. By use of interchangeable nozzle blocks the Mach number can be varied from 1.41 to 2.20. The dewpoint of the tunnel is held at 244° K or less to avoid any effects of condensation.

The probe pressures and nozzle stagnation pressure were measured with individual pressure transducers. Nozzle-exit static pressure was one of a group of pressures that was measured on pressure-scanning units. Probe longitudinal and lateral locations were

determined from position potentiometers. All instrumentation outputs were digitized and recorded on punch cards.

TESTS

Cylindrical Afterbody Tests

In order to obtain an indication of the support-strut interference effects, surface pressure distributions and boundary-layer pressure profiles were measured on the cylindrical afterbody. Surface pressure distributions were obtained for model lengths of 113.28 centimeters and 119.38 centimeters. Boundary-layer profiles were measured at five peripheral stations ($\phi = 0^\circ, 45^\circ, 90^\circ, 135^\circ, \text{ and } 180^\circ$) at longitudinal stations 104.14 centimeters and 110.29 centimeters. These model lengths and locations for measuring the boundary-layer profiles essentially bracketed the range of model lengths and location of the boattail juncture for the various nozzles investigated. Tests were also made on a sting-supported model which was identical to the jet-engine exhaust-nozzle simulator to obtain support-strut interference-free external-surface pressure distributions. Wind-tunnel free-stream conditions are summarized in the following table:

M	$p_{t,\infty}$, kN/m	$T_{t,\infty}$, °K	R
2.20	103.4	316.67	1.55×10^6
2.20	117.2	316.67	1.75
2.20	137.9	316.67	2.06

Tests were conducted with boundary-layer transition fixed 2.54 centimeters downstream from the nose of the models with a 0.25-centimeter-wide strip of No. 80 carborundum grit.

Conical-Probe Calibration

During phase I, the conical probe was only calibrated at a Mach number of 2.20, at angles of attack and roll of 0° , and at several longitudinal and lateral positions in the wind tunnel. Prior to phase II of the flow-field-survey investigation, the conical probe was calibrated at angles of attack from about -10° to 10° and roll angles of 0° and 180° at three Mach numbers. These three Mach number tests were made only to obtain the variation of the probe quantities with Mach number. The probe was also traversed longitudinally through the wind tunnel over a distance of about 50.8 centimeters. Wind-tunnel free-stream conditions for the conical-probe calibrations are summarized in the following table:

M	$P_{t,\infty}$, kN/m ²	$T_{t,\infty}$, °K	R
1.41	124.1	316.67	2.62×10^6
2.01	124.1	316.67	2.05
2.20	124.1	316.67	1.86

Flow-Field Surveys

Phase I.- Flow-field surveys during phase I were made at a Mach number of 2.20, a stagnation pressure of 124.1 kN/m², a stagnation temperature of 316.67° K, and a Reynolds number of 1.86×10^6 based on the model maximum diameter. Only the flow field surrounding nozzle 4 with the jet off and with the jet exhausting from the nozzle at an exit static-pressure ratio of 1.093 was measured at a radial station $z/D = 1.001$ during this phase of the investigation. This jet static-pressure ratio (1.093) was the maximum at which tests could be conducted during this phase because of a lack of sufficient scavenging capabilities in the Langley 4- by 4-foot supersonic pressure tunnel.

Because of limitations in the flow-survey traverse mechanism, the probe vertical position in the wind tunnel could not be adjusted to allow measurements in the horizontal plane through the model centerline; these tests were therefore made with the probe in a horizontal plane 9.02 centimeters above the model centerline. Boundary-layer transition was fixed as previously mentioned.

Phase II.- Flow-field surveys during phase II were also made at a Mach number of 2.20, a stagnation pressure of 124.1 kN/m², a stagnation temperature of 316.67° K, and a Reynolds number of 1.86×10^6 based on model maximum diameter. Boundary-layer transition was fixed as previously mentioned.

A complete longitudinal survey at $z/D = 1.00$ in the flow field of the jet-engine exhaust-nozzle simulator was made during this phase by moving the entire probe actuator forward longitudinally in the wind tunnel. This required locating the actuator at two additional forward locations such that surveys at adjacent positions overlapped, thereby providing a check on the repeatability of the data. The conical probe for this phase was always located in the horizontal plane of the nacelle centerline, and all surveys were made in that area of the wind tunnel opposite to the simulator support strut.

Surveys in the flow field surrounding the two equivalent solid bodies calculated from the phase I data were made at a radial location of $z/D = 1.00$. In addition flow-field surveys were made for seven nozzle configurations with jet exit static-pressure ratios as high as 2.236 at $z/D = 1.00$. Some limited measurements were made at other radial locations to assist in locating and determining the slope of the various shock waves in the flow fields surrounding the various configurations. Measurements were made in the

flow field of nozzle 4 with the jet operating at $p_j/p_\infty = 1.094$ so as to compare this data with the phase I data. (The difference in jet static-pressure ratio indicated (1.093 to 1.094) is within the accuracy of setting the jet operating conditions.)

DATA REDUCTION

The task of obtaining the Mach number and flow angularity from the four measurements of static pressure and the one measurement of impact pressure on the conical probe is complicated by the fact that one quantity must be known in order to determine the other. Reference 9 indicates that these quantities can be approximated with little error by the following power series if the appropriate constants are used

$$M = a_1 + a_2 \left(\frac{p_{t,i}}{p_{p,av}} \right) + a_3 \left(\frac{p_{t,i}}{p_{p,av}} \right)^2 + \theta^2 \left[a_4 + a_5 \left(\frac{p_{t,i}}{p_{p,av}} \right) + a_6 \left(\frac{p_{t,i}}{p_{p,av}} \right)^2 \right] \quad (1)$$

$$\theta_v = \left(b_1 + \frac{b_2}{M} + \frac{b_3}{M^2} \right) \frac{\Delta p_{p,v}}{p_{t,i}} \quad (2)$$

$$\theta_h = \left(b_1 + \frac{b_2}{M} + \frac{b_3}{M^2} \right) \frac{\Delta p_{p,h}}{p_{t,i}} \quad (3)$$

where

$p_{t,i}$	impact or stagnation pressure measured by probe
$p_{p,av}$	average of four static pressures measured on probe
$\Delta p_{p,v}$	difference in static pressures measured by orifices in vertical plane of probe
$\Delta p_{p,h}$	difference in static pressures measured by orifices in horizontal plane of probe
θ_v	flow angle in probe vertical plane
θ_h	flow angle in probe horizontal plane
θ	flow angle of probe

Since the flow angles θ_v and θ_h are in general small, the flow angle θ can be approximated by

$$\theta \approx \sqrt{\theta_v^2 + \theta_h^2} \quad (4)$$

In the present tests the constants a_m and b_n ($m = 1, 2, \dots, 6$; $n = 1, 2, 3$) in equations (1) to (3) were obtained with data from probe calibrations made in the wind tunnel in combination with data from the cone tables of references 10 to 12. Equations (1) to (4) are solved for Mach number and flow angularity by the following iteration procedure. An assumed value of the local Mach number is used to calculate the flow angle θ with equations (2) to (4). Then with this value of θ a new value of the local Mach number is calculated from equation (1). The procedure is repeated always by starting with the last calculated value of M until the calculated values of Mach number and flow angle do not change in successive iterations.

RESULTS AND DISCUSSION

Effect of Model Support Strut

The surface pressure distributions obtained on the jet-engine exhaust-nozzle simulator at a free-stream Mach number of 2.20 are presented as figure 5. These data indicate that there is essentially no effect of the support strut on the surface pressure distribution of the simulator. (The model lengths shown in figure 5 essentially bracket the range of model lengths tested in the present investigation.) The pressure gradient on the conical forebody of the sting-supported model is probably associated with the Mach number gradient just ahead of the tunnel test section. With the exception of these pressures, the measured surface pressures agree very well with those predicted by the method of characteristics.

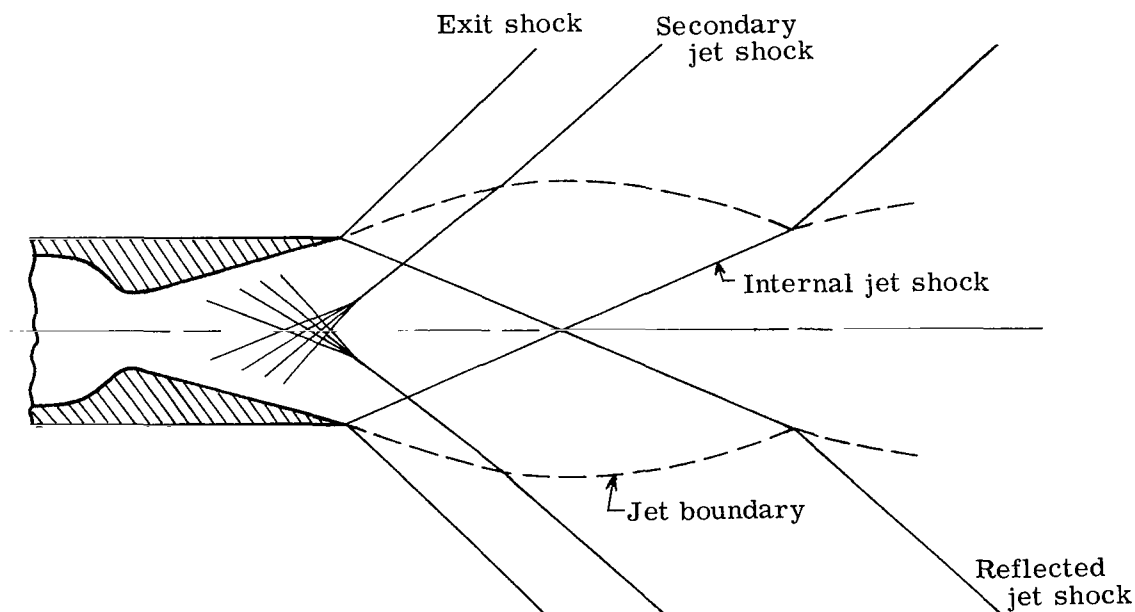
Boundary-layer stagnation-pressure profiles measured at $x/D = 6.833$ and 7.200 are presented as figures 6(a) and 6(b), respectively. From $\phi = 0^\circ$ to $\phi = 135^\circ$ there is essentially no effect of the support strut on the boundary-layer total-pressure profiles. However, as a result of the wake downstream of the strut, large defects in the total pressures occur at $\phi = 180^\circ$. There appears to be only small effects of varying the Reynolds number, based on body diameter, from 1.55×10^6 to 2.07×10^6 on the boundary-layer profiles.

Experimental Flow-Field Interference Signatures

The Mach number, flow angle, and pressure distributions measured one body diameter from the centerline of nozzle 4 during phase I of the investigation are presented as figure 7. The Mach number, flow angle, and pressure distributions measured one body

diameter from the axis of the 14° cone-cylinder forebody of the jet-engine exhaust-nozzle simulator during phase II are presented in figure 8. The effects of the ratio of jet static pressure to free-stream static pressure on the interference flow-field signatures resulting from each of the seven nozzle configurations tested during phase II are presented as figure 9. In figure 10 is shown a comparison of the flow-field signatures measured during phases I and II for nozzle 4 at a jet static-pressure ratio of 1.094. As can be seen, there is essentially no difference between the measurements made in the two phases of the experimental investigation.

In general the jet-plume interference signatures are characterized by a jump in the Mach number, flow angle, and pressure across the exit shock wave, and then a gradual expansion of the flow. Then, with the exception of nozzles 2 and 6, a weak secondary shock is encountered followed by a further expansion of the flow. A rather detailed study was made to determine the origin of the secondary shock wave. Shadowgraphs of the jet-plume shock system indicate that this secondary shock wave is not the result of the internal jet shock interacting with the jet boundary. See following sketch of the shock pattern surrounding the nozzle:



Total-pressure surveys presented as figure 11 indicate that the secondary shock originates inside the nozzle. This shock therefore is probably caused by a coalescence of compression waves following a rapid expansion behind the geometric nozzle throat. (See ref. 13.) With the exception of nozzle 2, the surface pressure distributions of nozzles 1 to 5 have a rapid expansion downstream of the geometric nozzle throat. (See fig. 12.)

Sufficient data are not available near the throat of nozzles 6 and 7 to make any definite conclusions. However there is evidence of an internal nozzle shock at $x_n/D \approx 0.2$ in nozzle 7.

Because of test limitations the surveys of the interference flow fields for the jets exhausting from the various nozzles were not made sufficiently far downstream to locate the trailing jet shock.

Verification of Analytical Method of Calculating Equivalent Solid Bodies

Comparison of calculated body shape with actual body shape.- In order to obtain an indication of the accuracy of the present method of calculating the equivalent solid body (see appendix A), the Mach number and flow-angle distributions measured one body diameter from the axis of the jet-engine exhaust-nozzle simulator (fig. 8) have been used to calculate the equivalent solid body producing these flow-field distributions. (The data of figs. 9(d), 9(f), and 9(g) upstream of the jet exit shock wave were also used in these calculations.) The comparison shown in figure 13(a) indicates good agreement between the calculated equivalent body shape and the actual body shape. As indicated previously, the present method of calculating the equivalent body is based on inviscid theory. However, in the real flow, boundary-layer displacement effects will alter the flow-field signatures somewhat. The calculated equivalent body shapes then will include the boundary-layer displacement thickness. Therefore in figure 13(b) the calculated equivalent bodies corrected for boundary-layer displacement thickness are compared with the actual coordinates of the jet-engine exhaust-nozzle simulator. In order to calculate the boundary-layer displacement thickness, the momentum thickness was first calculated by the method of reference 14 as modified by reference 15. (The Mach number distribution required along the body surface by this method was determined in the calculations of the equivalent solid bodies.) The equations given in the appendix of reference 16 were then used to calculate the displacement thickness from the momentum thickness. (A seventh-power velocity profile was assumed.) As shown in figure 13(b) this correction for boundary-layer displacement thickness substantially improves the agreement between the calculated equivalent body shape and the actual body shape.

However a discrepancy still exists between the calculated body shape and the actual body shape of the conical forebody. An analysis of the data of figure 8 indicates that the location of the bow shock wave and the pressure rise across this shock wave differ from the predictions of cone theory for a 14° cone at $M_\infty = 2.20$. In fact, these parameters are closer to the predictions of cone theory for a 15° cone at $M_\infty = 2.20$. The resulting calculated equivalent body shape is therefore essentially a 15° cone. The most likely cause of these discrepancies is the location of the nose of the simulator in the Mach number gradient just ahead of the tunnel test section. (A free-stream Mach number of 2.15 would give the observed shock location and pressure jump with a 14° cone.) There are

several other possible causes of the observed discrepancies, such as cone nose bluntness, free-stream flow angularity, and three-dimensional effects due to the strut; however a study has indicated that the possible magnitude of these effects is not sufficient to account for the aforementioned discrepancies.

There also appears to be a discrepancy between the calculated location and the actual location of the origin of the 10° boattail afterbody. (See fig. 13(b).) This difference can partly be accounted for because the curvature of the characteristics of the flow in the boundary layer is not accounted for in the present inviscid method of calculating the equivalent body shape. As a result the apparent origin of the Prandtl-Meyer expansion fan is upstream of the real origin.

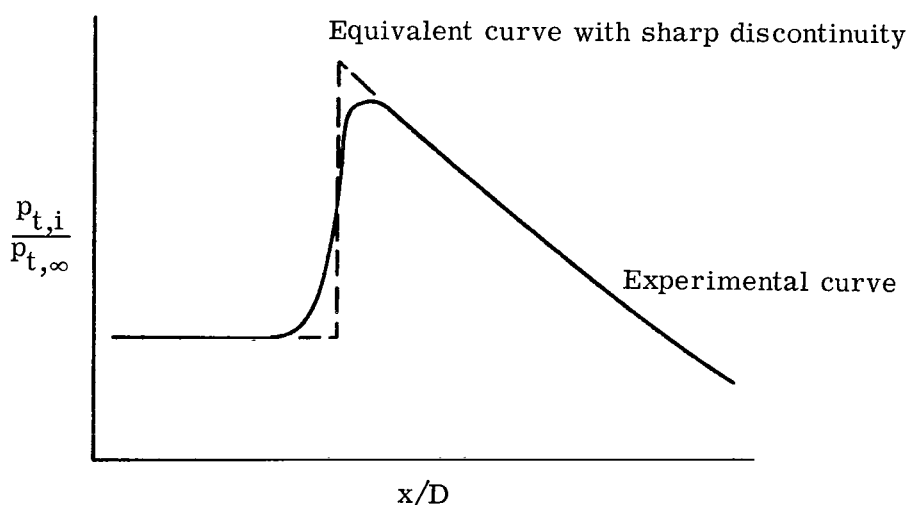
The preceding discussion has indicated that the present method provides an adequate means of calculating the equivalent body shape producing a measured or specified Mach number and flow-angle distribution.

Comparison of effective solid body and jet-plume interference flow fields.- The Mach number and flow-angle distributions measured during phase I for nozzle 4 (fig. 7) have been used to calculate the effective solid body of the wake (that is, with the jet off) of the jet-engine exhaust-nozzle simulator and the jet equivalent solid body for the jet exhausting from nozzle 4 at a jet static-pressure ratio of 1.094. In calculating the wake equivalent solid body (fig. 14) the effects of boundary-layer displacement were included. However, since the data measured about the cone-cylinder forebody were not available when these bodies were calculated, the boundary-layer displacement thicknesses calculated from the profiles given in figure 6 were used to determine the initial radius and slope of the equivalent body streamline of the nozzle. In order to obtain the wake equivalent solid body the increment between the calculated body streamline radius and the nozzle radius at the exit (that is, essentially the boundary-layer displacement thickness at the exit) was subtracted from all calculated streamline radii downstream of the nozzle exit. Experimental measurements made for this wake equivalent solid body during phase II are compared in figure 15 with the phase I data from which the equivalent solid body was calculated. In general good agreement exists between the flow-field signatures produced by the wake equivalent solid body and the wake. However the location of the initial expansion wave for the equivalent body appears to be somewhat in error. This discrepancy probably results, at least partly, because the velocity gradient in the boundary layer causes significantly more curvature of the characteristics of the flow near the body surface than the present inverse inviscid procedure calculates. As mentioned previously, neglecting the characteristic curvature results in the apparent origin of the initial expansion wave being upstream of the real origin (the nozzle exit).

The calculated jet equivalent body shape for the jet exhausting from nozzle 4 at a static-pressure ratio of 1.093 is presented as figure 16. The jet exit shock was assumed

to be attached to the nozzle-exit lip and to pass through a point one body diameter from the axis such that the pressure rise calculated from the slope and the conditions at the last data point ahead of the shock would correspond to the pressure rise determined by extrapolating the pressure data downstream to the shock. In calculating the jet equivalent body shape the boundary-layer displacement thickness was not included in the radius of the initial body streamline. The comparison presented as figure 17 indicates fair agreement between the flow-field signatures measured for the jet equivalent solid body and the corresponding jet plume. However there is a longitudinal displacement of the equivalent body signatures and the strength of the exit shock is not simulated correctly. These differences could have been caused by not including boundary-layer displacement thickness or by using an incorrect location and slope for the exit shock wave in the calculations of the jet equivalent solid body. In order to determine the effect of these factors, an analytical study has been made by calculating equivalent solid bodies with different shock angles and locations and by including the effects of boundary-layer displacement.

During the phase II tests very closely spaced data points were obtained in the region of the shock waves in the flow, thereby providing a means of more precisely determining the shock location. The shock locations for the interference signatures measured during phase II were determined from impact pressure distributions similar to those presented in figure 11. (The impact pressure distributions were chosen since these measurements would have a smaller error resulting from the finite size of the probe.) These distributions have some rounding in the vicinity of the shock waves as a result of the finite size of the probe instead of the characteristic discontinuity. The shock therefore was located such that the area under a curve with a discontinuity at the shock would equal the area under the rounded experimental curve as shown in the following sketch:



The shock strength (that is, slope) was then determined by extrapolating the experimental pressure distributions upstream and downstream to the shock wave to determine the static-pressure rise across the shock. This static-pressure rise and the extrapolated Mach number ahead of the shock were used to calculate the shock angle. The shock angles and locations calculated for the phase I and phase II data are presented in table II. Boundary-layer displacement effects were included in the phase II calculations by extending the body streamline presented in figure 13(a) downstream.

As shown in figure 18(a) the body shape calculated from the phase II data is considerably larger in diameter than the body shape calculated from the phase I data. It is likely, since the initial slope of the jet equivalent body shape is also greater for the phase II calculations, that the phase II equivalent body shape would provide an interference pressure distribution closer to the measured jet pressure signature. As indicated previously, the differences shown in figure 18(a) could have been caused by not including boundary-layer displacement thickness or by using an incorrect location and slope for the exit shock wave in the calculations of the phase I jet equivalent solid body. The effects of these factors on the jet equivalent solid body are shown in figures 18(b) to 18(d). The comparison shown in figure 18(b) indicates that changing the exit shock angle from 28° to 29° has essentially no effect on the calculated body shape, thereby indicating that the disagreement shown in figure 18(a) is not caused by the difference in calculated shock angle. (See table II.) Omission of the boundary-layer displacement thickness (see fig. 18(c)) in the calculation of the equivalent body shape (as was done in the phase I calculations) essentially results only in a longitudinal translation of the effective body. Since the interference signatures measured during phase I and phase II are the same, the only remaining factor to account for the differences indicated in figure 18(a) is the location of the exit shock wave. Therefore in figure 18(d) the equivalent bodies calculated from the phase I and phase II data using the phase I exit shock wave are compared, and in figure 18(e) the equivalent bodies calculated from the phase I and phase II data using the phase II exit shock are compared. The agreement in the calculated equivalent body shape shown in these comparisons indicates that the differences shown in figure 18(a) are most likely caused by the different shock locations used in the calculations. Therefore the differences in the interference signatures for the jet plume and the jet equivalent solid body probably result from using the wrong shock location in calculating the jet equivalent body. A more correct calculation of the jet equivalent body shape would probably have provided better agreement in the interference signatures.

These comparisons have indicated that the concept of representing a jet plume by a corresponding equivalent solid body shape is valid. Also the comparisons have shown that the present method of calculating the jet equivalent solid body is adequate provided that the location and slope of shock waves in the flow field are accurately determined.

Comparison of Jet Equivalent Solid Bodies With Inviscid Jet Boundaries

A comparison of the jet equivalent solid bodies with the corresponding inviscid jet boundaries is shown in figure 19 for the seven nozzles of the present investigation operating at various jet static-pressure ratios. The inviscid jet boundaries were calculated by the method of reference 4. Also shown in figure 19 are several inviscid jet boundaries calculated by a method of characteristics solution assuming uniform external flow upstream of the nozzle exit and conical flow inside of the nozzle. As can be seen, the two inviscid solutions are in close agreement.

The jet equivalent solid bodies have been calculated by the method developed herein from the data presented as figure 9. The shock angles and locations used in the calculations are given in table II. These jet equivalent bodies presented in figure 19 have been corrected for the boundary-layer displacement thickness at the intersection of the exit shock wave with the nozzle surface. For those nozzles where the experimental flow-field signatures indicate a secondary shock wave, the jet equivalent solid bodies have a discontinuous change in slope downstream of the nozzle exit.

The inviscid jet boundary is considerably larger in diameter than the corresponding jet equivalent solid body with the difference increasing with longitudinal distance downstream of the jet exit.

Calculation of Jet-Plume Interference on Wave Drag, Lift, and Sonic-Boom

Pressure Signature of Supersonic Airplanes

As indicated previously the methods of calculating the zero-lift wave drag (ref. 1) and the sonic-boom pressure signatures (refs. 2 and 3) of a supersonic airplane generally represent the jet exhausting from an engine nacelle as a cylinder extending downstream to infinity. In general, however, the jet-plume shape will differ from a cylinder. These methods therefore neglect the interference effects which may result from these deviations of the jet exhaust from a cylinder. A conceptual procedure to calculate these jet-plume interference effects is as follows: (1) Include a jet equivalent body in the geometry of the airplane to represent the jet exhaust plume; (2) use a near field method such as a three-dimensional method of characteristics or an approximate method similar to the method of reference 17 to calculate the jet-plume induced pressures on adjacent airframe surfaces; and (3) integrate these induced pressures to determine the interference drag and lift. At present, unfortunately, there is no near field method readily available to calculate the induced pressures. However from the comparisons shown in figure 19 and the pressure data of figure 9, it can be inferred that the drag of an airplane can be reduced by jet-plume interference provided that favorable jet-induced pressures act on appropriate adjacent airframe surfaces (that is, increased pressures act on rearward facing surfaces and decreased pressures act on forward facing surfaces). Figure 19

shows that the use of the inviscid jet boundary calculated by the method of characteristics would greatly overpredict these effects.

The jet equivalent solid bodies calculated for jets exhausting from the isolated nacelle of the present investigation (fig. 19) can be used in these calculations for airplanes with podded engines operating at similar conditions provided that a method of calculating the induced pressures is available. However, in using these isolated-nacelle jet equivalent solid bodies, the effects of the airplane on the plume shape are neglected. In addition, if there is more than one engine, the effects of the jet plumes on each other are neglected. Since these effects would vary with airplane geometry, there does not seem to be any readily available method of correcting the jet equivalent solid bodies for the effects of airplane geometry and other jet plumes on the jet plume under consideration. Hopefully the effects of neglecting these factors will only have a small effect on the total drag of the airplane. In addition to the preceding considerations the following restrictions should be adhered to when using the jet equivalent solid bodies calculated from isolated-nacelle data: (1) The jet exhaust from the engine nacelle is parallel to the free stream; (2) the engine nacelles are axially symmetric; (3) the jet plumes when there are more than one do not interact; and (4) the jet plumes do not intersect or wash adjacent airframe surfaces.

It should also be emphasized here that the jet equivalent solid bodies presented herein were determined from flow-field signatures for cold air jets exhausting from a specific isolated nacelle. Changes in such factors as the nacelle shape, the characteristics of the external and internal boundary layer at the nozzle exit, the composition of the exhaust gases, the ratio of specific heat of the jet and jet temperature may alter the shapes of equivalent bodies and the preceding result considerably.

The effects of jet plumes on the sonic-boom pressure signatures of supersonic airplanes can be determined by including the appropriate jet equivalent solid body in the geometry of the airplane and by using the theoretical method of references 2 and 3. In order to obtain an indication of these effects, the sonic-boom pressure signatures for a fighter-type airplane with two podded engines and a supersonic-transport configuration with four podded engines have been calculated. The results of these calculations shown in figure 20 indicate that there is considerable effect on the trailing-shock-wave system resulting from the jet plume with the effects increasing with jet pressure ratio. However these effects are a near field effect, and calculations of the far field N-wave pressure signatures indicated that for the cases considered there would be no effect of the jet plume.

CONCLUDING REMARKS

An inverse application of the method of characteristics for potential axially symmetric flow has been developed to calculate an equivalent solid body which will produce the same interference pressure field as an axially symmetric jet exhausting into a supersonic stream. The effects on sonic-boom pressure signatures of supersonic airplanes can be determined with present analytical methods by representing jet exhaust plumes with the corresponding jet equivalent solid body. The jet-plume interference effects on adjacent airframe surfaces can also be determined provided adequate near field methods of calculating induced flow fields become available.

An experimental investigation has been made at a free-stream Mach number of 2.20 to obtain measurements of local Mach number, flow angle, and pressure in the external flow field surrounding cold air jets exhausting from various axially symmetric nozzle configurations. Flow-field measurements were also made for the jet-engine nacelle simulator (a 14° cone-cylinder body) and for two jet equivalent solid bodies calculated from the jet-plume flow-field data. A comparison of the calculated body shape corrected for boundary-layer displacement thickness indicated excellent agreement with the actual body geometry of the engine simulator. The good agreement between the flow-field signatures produced by the two jet equivalent solid bodies and the corresponding jet plumes has verified the present concept of representing a jet plume by an equivalent solid body.

Comparisons have shown that the calculated radius of the theoretical inviscid jet boundaries for all nozzles and jet pressure ratios of the present tests increase considerably faster with longitudinal distance downstream of the nozzle exit than the corresponding jet equivalent solid bodies. Calculations have also shown considerable effects of the jet plumes on the trailing-shock-wave system in the near field sonic-boom signatures of two representative airplanes with podded engines.

Langley Research Center

National Aeronautics and Space Administration,

Langley Station, Hampton, Va., October 1, 1969.

APPENDIX A

METHOD OF CALCULATING EQUIVALENT BODY SHAPE

By Lawrence E. Putnam

TECHNIQUE

A semiempirical procedure has been developed and programed for a digital computer to calculate the equivalent solid body shape that will produce the same interference flow field as a jet expanding into a supersonic stream. This procedure, which has been restricted to the case where the flow about the engine nacelle and jet plume can be considered axially symmetric, is based on an inverse application of the method of characteristics; that is, the body shape is calculated from specified conditions in the flow field rather than the flow-field quantities being calculated from the body shape (the direct solution). (A description of the axially symmetric method of characteristics for potential flow from reference 18 is presented briefly in appendix B.) For simplicity, in addition to the assumptions inherent in the method of characteristics for potential flow (that is, the flow is everywhere supersonic, inviscid, and isentropic), the assumption has been made in the present analysis that all shock waves in the flow field are linear. As a result of the assumption of linear shock waves, the present analysis is probably limited to the relatively near field. If strong curvature of the shock waves in the flow should occur, the assumption of irrotational flow downstream of the curve shocks would be invalid. In such cases the present procedure would have to be modified to account for rotational flow.

In concept the procedure developed to calculate the equivalent solid body shape is as follows. From specified conditions along some initial line in the flow field of an engine nacelle and jet plume, a characteristic net is calculated toward the axis of symmetry. Through this characteristic net the coordinates of the streamline which represents the effective solid body are calculated.

Characteristic-Net Calculation

As indicated in reference 19 and the equations of appendix B, specification of the velocity ratio W and the flow angle θ as continuously differential functions along some noncharacteristic line will permit a unique solution for the characteristic net in the flow-field domain enclosed by the characteristics from each end of the noncharacteristic line. For adiabatic flow W and μ can be determined from the local Mach number. (See ref. 20.) Therefore the present method requires that the variation of Mach number and flow angle along some noncharacteristic line in the flow field of the nacelle and jet plume be determined. These quantities can be calculated along a noncharacteristic line just

APPENDIX A

behind a bow shock wave from the free-stream conditions by using the Rankine-Hugoniot equations provided that the location and slope of the shock wave are known. In the flow field downstream of the bow shock wave these quantities must be experimentally measured. The noncharacteristic line along which the Mach number and flow angle are determined must be such that the characteristic from each end of the line encloses the region in the flow field where the equivalent solid body streamline is located.

In regions of the flow field where there are no shock waves, the characteristic net can be calculated from an initial line of the type where W and θ are specified as continuously differential functions. An outline of the characteristic-net computational procedure is as follows. The coordinates and flow properties W , θ , and μ at point (1,2) (see fig. 21(a) or 21(b)) are calculated from the known conditions at points (1,1) and (2,2) on the initial line by the field point calculation procedure of the method of characteristics given in appendix B. Then the conditions at point (2,3) are calculated from the conditions on the initial line at points (2,2) and (3,3) and the conditions at point (1,3) are calculated from the conditions at points (1,2) and (2,3). In a like manner, by proceeding downstream, each first family characteristic (that is, the characteristic with slope $\frac{dr}{dx} = \tan(\theta + \mu)$) through each point on the initial line is calculated.

When a secondary shock such as a nozzle-exit shock is encountered in the flow field, special treatment in the characteristic-net calculation is required since the velocity ratio W and the flow angle θ are discontinuous across the shock wave. The calculation procedure required to insert a shock wave in the characteristic net is illustrated in figure 21(c). The characteristic net ahead of the shock wave is calculated until the first family characteristic through the last point on the initial line before the shock wave (for example, point (9,J) in fig. 21(c)) is obtained. The coordinates and slope of the surface streamline are calculated downstream to this characteristic. (The method of calculating the surface or equivalent body streamline is discussed subsequently.) From the last calculated surface streamline point in the characteristic net ahead of the shock wave, a fictitious streamline is extrapolated linearly downstream past the shock wave. This fictitious streamline provides a noncharacteristic boundary at which the flow angle θ is specified as a continuously differential function. Then by using this boundary and the last first family characteristic ahead of the shock wave, the characteristic net that would result if there was no shock wave in the flow field is calculated. At the intersection of the second family characteristics (that is, characteristics with slope $\frac{dr}{dx} = \tan(\theta - \mu)$) with the fictitious streamline the surface point calculation as given in appendix B is used. Next the intersection of the shock wave with the fictitious characteristic net is determined, and the values of W , θ , and μ just in front of the shock wave are determined by linear interpolation between points in the fictitious characteristic net. The location and slope of the shock wave must be determined for this analysis by experimental

APPENDIX A

measurement. The flow quantities just behind the shock wave are then calculated from the Rankine-Hugoniot relations (ref. 20). Since these flow quantities just behind the shock wave are not on a characteristic, a new characteristic net downstream of the shock wave can be calculated in the same manner as previously described.

Effective Body Streamline Calculations

The calculation of the surface or effective body streamline requires an initial starting point at which the slope of the streamline is known. By starting with this point, the path of the surface streamline through the characteristic net is obtained by a step-by-step interpolation procedure. From the initial point the streamline is extrapolated linearly downstream at the initial slope until it intersects a characteristic. At this point the slope of the streamline is calculated by linearly interpolating between points on the characteristic for the flow angle θ . The streamline is again extrapolated downstream at the new slope from the intersection point until it intersects the next characteristic and a new streamline slope is calculated. This step-by-step procedure is continued until the path of the streamline is computed through the characteristic net. At secondary shock waves in the flow the discontinuous change in slope is determined with the oblique shock relations (ref. 20).

EXAMPLE CALCULATION

In order to illustrate and verify the procedure used to calculate the equivalent surface streamline from flow-field measurements, the flow field for a 14° cone-cylinder body at a Mach number of 2.20 has been calculated by the axially symmetric method of characteristics. Theoretical values of the local Mach number, flow deflection angle, and ratio of the local velocity to the limiting velocity just behind the initial shock wave and at one body diameter from the axis of symmetry have been determined. By starting with these theoretical flow quantities the effective body streamline has been calculated by the aforementioned procedure. As can be seen in figure 22, the calculated equivalent streamline agrees very well with the actual body shape. This result indicates that, at least theoretically, the procedure developed to calculate the equivalent body streamline from measurements of the flow-field quantities M and θ will provide a reasonable approximation to the actual body shape.

As indicated in appendix B an iteration procedure is necessary to calculate the characteristic net. In order to obtain an indication of the number of iterations required for convergence of the characteristic-net solution, the effective surface streamline of the 14° cone-cylinder body at $M_\infty = 2.20$ was obtained by using various numbers of iterations to calculate the characteristic net. As can be seen in figure 23, the solution rapidly converges as the number of iterations increases. However for this case the

APPENDIX A

radius of the effective surface streamline converges to a value approximately 1 to 3 percent larger than the exact radius of the body at a given longitudinal location depending on the value of x/D . From this analysis it is seen that only three or four iterations will normally be required for convergence of the characteristic-net calculation.

APPENDIX B

METHOD OF CHARACTERISTICS THEORY

The axially symmetric method of characteristics for supersonic potential flow is given in many references. However, since the various references give slightly different methods of solution for the basic equations, the present procedure which is based on the method given in reference 18 is now given.

The equations necessary to calculate the conditions at a field point C (see fig. 24) are:

Along the characteristic line AC

$$\frac{dr}{dx} = \tan(\theta + \mu) \quad (B1)$$

$$\cot \mu \frac{dW}{W} - d\theta - \frac{\sin \mu \sin \theta}{\cos(\theta + \mu)} \frac{dx}{r} = 0 \quad (B2)$$

and along the characteristic line BC

$$\frac{dr}{dx} = \tan(\theta - \mu) \quad (B3)$$

$$\cot \mu \frac{dW}{W} + d\theta - \frac{\sin \mu \sin \theta}{\cos(\theta - \mu)} \frac{dx}{r} = 0 \quad (B4)$$

Writing these equations in finite difference form, since they can only be solved by a step-by-step numerical procedure, gives

$$\frac{r_C - r_A}{x_C - x_A} = K_1 \quad (B5)$$

$$K_2(W_C - W_A) - (\theta_C - \theta_A) - K_3(x_C - x_A) = 0 \quad (B6)$$

$$\frac{r_C - r_B}{x_C - x_B} = K_4 \quad (B7)$$

$$K_5(W_C - W_B) + (\theta_C - \theta_B) - K_6(x_C - x_B) = 0 \quad (B8)$$

APPENDIX B

Since the conditions at points A and B are known, as a first approximation

$$\left. \begin{aligned} K_1 &= \tan(\theta_A + \mu_A) \\ K_2 &= \frac{\cot \mu_A}{W_A} \\ K_3 &= \frac{\sin \mu_A \sin \theta_A}{r_A \cos(\theta_A + \mu_A)} \\ K_4 &= \tan(\theta_B - \mu_B) \\ K_5 &= \frac{\cot \mu_B}{W_B} \\ K_6 &= \frac{\sin \mu_B \sin \theta_B}{r_B \cos(\theta_B - \mu_B)} \end{aligned} \right\} \quad (B9)$$

As a second approximation

$$\left. \begin{aligned} K_1 &= \frac{1}{2} \left[\tan(\theta_A + \mu_A) + \tan(\theta_C + \mu_C) \right] \\ K_2 &= \frac{1}{2} \left(\frac{\cot \mu_A}{W_A} + \frac{\cot \mu_C}{W_C} \right) \\ K_3 &= \frac{1}{2} \left[\frac{\sin \mu_A \sin \theta_A}{r_A \cos(\theta_A + \mu_A)} + \frac{\sin \mu_C \sin \theta_C}{r_C \cos(\theta_C + \mu_C)} \right] \\ K_4 &= \frac{1}{2} \left[\tan(\theta_B - \mu_B) + \tan(\theta_C - \mu_C) \right] \\ K_5 &= \frac{1}{2} \left(\frac{\cot \mu_B}{W_B} + \frac{\cot \mu_C}{W_C} \right) \\ K_6 &= \frac{1}{2} \left[\frac{\sin \mu_B \sin \theta_B}{r_B \cos(\theta_B - \mu_B)} + \frac{\sin \mu_C \sin \theta_C}{r_C \cos(\theta_C - \mu_C)} \right] \end{aligned} \right\} \quad (B10)$$

where the quantities at point C are determined by the first approximation. In a similar way further approximations can be made by substituting into equation (B10) the latest calculated values of the quantities at point C. The iteration procedure should be continued until the position of point C does not change in successive iterations.

APPENDIX B

If the conditions at point D (fig. 24) are known, the flow quantities at the surface point E can be calculated from the equations

$$\frac{r_E - r_D}{x_E - x_D} = C_1 \quad (B11)$$

$$C_2(w_E - w_D) + (\theta_E - \theta_D) - C_3(x_E - x_D) = 0 \quad (B12)$$

where as a first approximation

$$\left. \begin{aligned} C_1 &= \tan(\theta_D - \mu_D) \\ C_2 &= \frac{\cot \mu_D}{w_D} \\ C_3 &= \frac{\sin \mu_D \sin \theta_D}{r_D \cos(\theta_D - \mu_D)} \end{aligned} \right\} \quad (B13)$$

Further approximations can be made as in the case for a field point calculation by letting

$$\left. \begin{aligned} C_1 &= \frac{1}{2} [\tan(\theta_D - \mu_D) + \tan(\theta_E - \mu_E)] \\ C_2 &= \frac{1}{2} \left(\frac{\cot \mu_D}{w_D} + \frac{\cot \mu_E}{w_E} \right) \\ C_3 &= \frac{1}{2} \left[\frac{\sin \mu_D \sin \theta_D}{r_D \cos(\theta_D - \mu_D)} + \frac{\sin \mu_E \sin \theta_E}{r_E \cos(\theta_E - \mu_E)} \right] \end{aligned} \right\} \quad (B14)$$

REFERENCES

1. Harris, Roy V., Jr.: An Analysis and Correlation of Aircraft Wave Drag. NASA TM X-947, 1964.
2. Carlson, Harry W.: Correlation of Sonic-Boom Theory With Wind-Tunnel and Flight Measurements. NASA TR R-213, 1964.
3. Middleton, Wilbur D.; and Carlson, Harry W.: A Numerical Method for Calculating Near-Field Sonic-Boom Pressure Signatures. NASA TN D-3082, 1965.
4. Englert, Gerald W.: Operational Method of Determining Initial Contour of and Pressure Field About a Supersonic Jet. NASA TN D-279, 1960.
5. Wang, C. J.; and Peterson, J. B.: Spreading of Supersonic Jets From Axially Symmetric Nozzles. Jet Propulsion, vol. 28, no. 5, May 1958, pp. 321-328.
6. Henson, J. R.; and Robertson, J. E.: Methods of Approximating Inviscid Jet Boundaries for Highly Underexpanded Supersonic Nozzles. AEDC-TDR-62-7 (Contract No. AF 40(600)-800 S/A 24(61-73)), Arnold Eng. Dev. Center, May 1962.
7. Korst, H. H.; and Chow, W. L.: Non-Isoenergetic Turbulent $Pr_t = 1$ Jet Mixing Between Two Compressible Streams At Constant Pressure. NASA CR-419, 1966.
8. Bonner, E.; and Nixon, J. A.: Wind Tunnel Testing Techniques for Integrated Airframe-Exhaust Nozzle Systems. Tech. Rep. AFFDL-TR-68-94, U.S. Air Force, July 1968.
9. Carlson, Harry W.: Measurements of Flow Properties in the Vicinity of Three Wing-Fuselage Combinations at Mach Numbers of 1.61 and 2.01. NASA TM X-64, 1959.
10. Staff of the Comput. Section, Center of Anal. (Under dir. of Zdeněk Kopal): Tables of Supersonic Flow Around Cones. Tech. Rep. No. 1 (NOrd Contract No. 9169), Massachusetts Inst. Technol., 1947.
11. Staff of Comput. Section, Center of Anal. (Under dir. of Zdeněk Kopal): Tables of Supersonic Flow Around Yawing Cones. Tech. Rep. No. 3 (NOrd Contract No. 9169), Massachusetts Inst. Technol., 1947.
12. Staff of Comput. Section, Center of Anal. (Under dir. of Zdeněk Kopal): Tables of Supersonic Flow Around Cones of Large Yaw. Tech. Rep. No. 5 (NOrd Contract Nos. 8555 and 9169), Massachusetts Inst. Technol., 1949.
13. Migdal, D.; and Kosson, R.: Shock Predictions in Conical Nozzles. AIAA J. (Tech. Notes), vol. 3, no. 8, Aug. 1965, pp. 1554-1556.

14. Englert, Gerald W.: Estimation of Compressible Boundary-Layer Growth Over Insulated Surfaces With Pressure Gradient. NACA TN 4022, 1957.
15. Jackson, Charlie M., Jr.; and Smith, Rudeen S.: A Method For Determining the Total Drag of a Pointed Body of Revolution in Supersonic Flow With Turbulent Boundary Layer. NASA TN D-5046, 1969.
16. Adcock, Jerry B.; Peterson, John B., Jr.; and McRee, Donald I.: Experimental Investigation of A Turbulent Boundary Layer at Mach 6, High Reynolds Numbers, and Zero Heat Transfer. NASA TN D-2907, 1965.
17. Mack, Robert J.: A Numerical Method for Evaluation and Utilization of Supersonic Nacelle-Wing Interference. NASA TN D-5057, 1969.
18. Sears, W. R., ed.: General Theory of High Speed Aerodynamics. Vol. VI of High Speed Aerodynamics and Jet Propulsion, Princeton Univ. Press, 1954.
19. Crandall, Stephen H.: Engineering Analysis. McGraw-Hill Book Co., Inc., 1956.
20. Ames Research Staff: Equations, Tables, and Charts for Compressible Flow. NACA Rep. 1135, 1953. (Supersedes NACA TN 1428.)

TABLE I.- EQUIVALENT SOLID BODY ORDINATES

x/D	r/D	x/D	r/D	x/D	r/D
Wake equivalent solid body					
6.667	0.5000	7.465	0.4922	7.856	0.4300
7.236	.5000	7.473	.4910	7.907	.4207
7.370	.5000	7.566	.4773	7.947	.4133
7.392	.4998	7.622	.4685	7.952	.4125
7.393	.4997	7.673	.4605	7.999	.4037
7.400	.4993	7.678	.4597	8.040	.3957
7.408	.4988	7.723	.4525	8.066	.3905
7.411	.4985	7.753	.4477	8.087	.3865
7.425	.4970	7.776	.4438	8.143	.3752
7.440	.4953	7.815	.4373	^a 8.165	^a .3710
7.451	.4942	7.837	.4333	^a 8.667	^a .2692
Jet equivalent solid body					
6.667	0.5000	7.953	0.5180	8.586	0.5093
7.433	.5000	7.978	.5180	8.600	.5090
7.496	.5047	8.030	.5178	8.661	.5072
7.545	.5077	8.033	.5178	8.681	.5067
7.570	.5088	8.088	.5173	8.733	.5055
7.606	.5107	8.119	.5170	8.734	.5053
7.645	.5122	8.156	.5163	8.793	.5035
7.670	.5132	8.193	.5157	8.820	.5027
7.725	.5148	8.285	.5135	8.857	.5013
7.727	.5150	8.287	.5140	8.908	.4993
7.785	.5163	8.359	.5115	8.922	.4988
7.799	.5165	8.430	.5117	8.982	.4962
7.847	.5173	8.466	.5113	8.988	.4958
7.871	.5175	8.511	.5107	^a 8.999	^a .4953
7.907	.5178	8.538	.5103	^a 9.500	^a .4717

^aThese points are coordinates extrapolated downstream of last point calculated from flow-field signatures.

TABLE II.- JET-PLUME SHOCK LOCATIONS AND ANGLES AT $z/D = 1.00$

Nozzle	p_j/p_∞	Exit shock		Secondary shock	
		x/D	ψ , deg	x/D	ψ , deg
1	0.962	8.664	29.1135	9.113	29.2316
1	1.414	8.590	30.7146	9.018	32.0176
2	1.375	8.638	30.4350	(a)	(a)
3	.935	8.495	28.4105	9.226	26.9670
3	1.358	8.418	30.0830	9.127	29.4003
4	.970	8.307	28.4374	(b)	(b)
^c 4	1.093	8.336	29.0546	(d)	(d)
4	1.094	8.261	28.7865	9.330	25.9184
4	1.284	8.238	29.3078	9.306	26.5401
4	1.912	8.160	31.7658	9.207	28.9694
4	2.326	8.117	31.9305	9.185	30.3204
5	1.071	8.326	28.0350	9.010	26.5575
5	1.400	8.241	30.0360	8.898	28.7804
5	2.008	8.173	30.8713	8.810	31.2137
6	1.011	8.593	25.5174	(a)	(a)
6	1.383	8.481	27.2643	(a)	(a)
6	2.003	8.374	29.0471	(a)	(a)
7	1.395	8.734	23.8019	9.331	27.4073
7	1.998	8.600	25.5609	9.253	28.5728

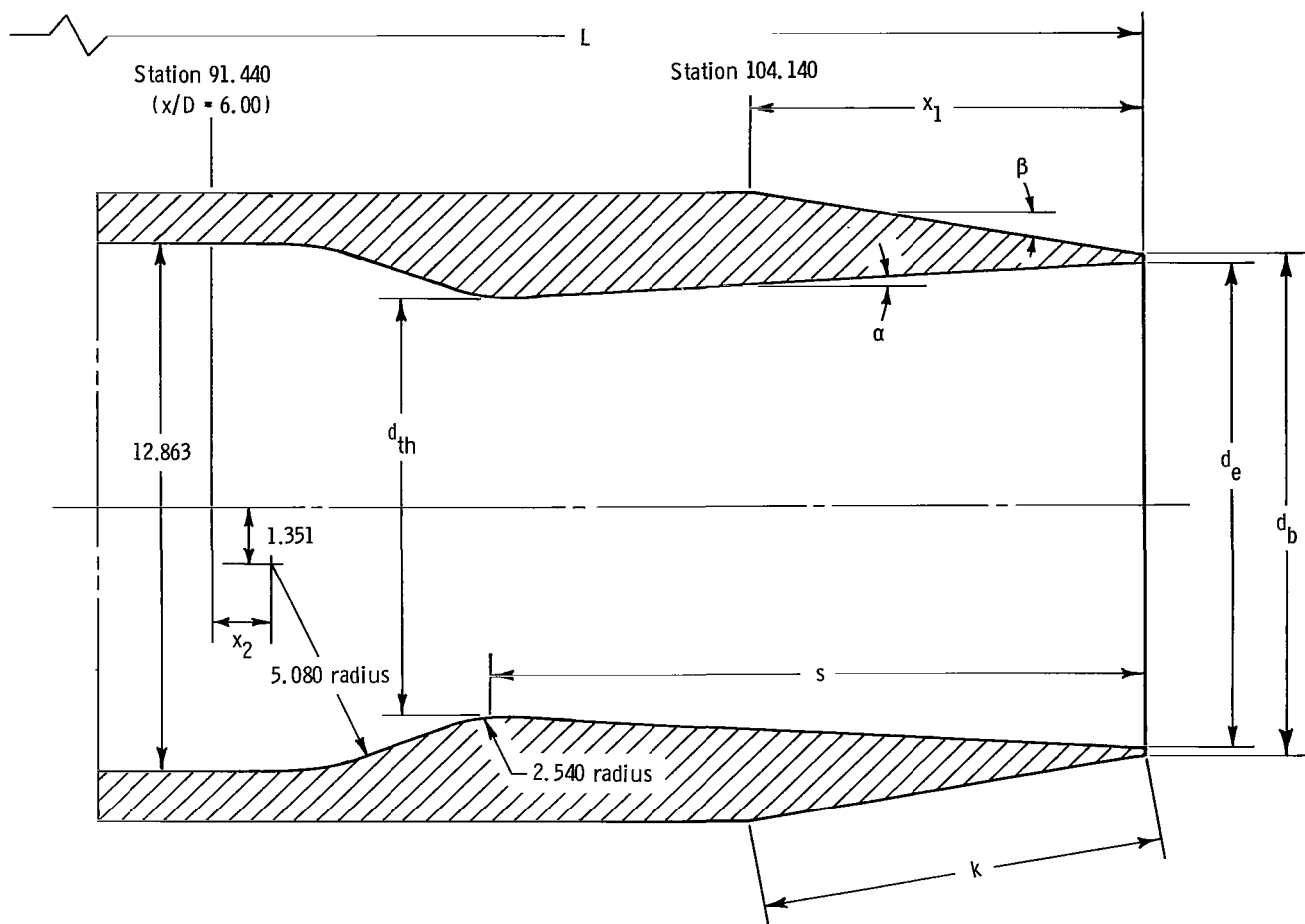
^aNo secondary shock.

^bInsufficient data to locate secondary shock.

^cPhase I data.

^dValues not calculated.

Figure 1.- Sketch of jet-engine exhaust-nozzle simulator. All dimensions in centimeters unless otherwise noted.



Nozzle	$M_{j,des}$	$\left(\frac{p_{t,j}}{p_{\infty}}\right)_{des}$	α , deg	β , deg	x_1	L	k	s	d_{th}	d_e	d_b	A_{th}	A_e	A_e/A_{th}	x_2
1	2.920	32.58	11.50	0	15.240	119.380	15.240	18.519	7.577	15.011	15.240	45.09	176.98	3.925	2.908
2	2.272	11.97	7.28	0	15.240	119.380	15.240	18.747	10.264	15.011	15.240	82.75	176.98	2.139	4.224
3	2.740	24.77	11.50	0	12.192	116.332	12.192	16.878	8.255	15.011	15.240	53.52	176.98	3.307	2.118
4	2.523	17.72	11.50	0	9.144	113.284	9.144	14.883	9.144	15.011	15.240	65.66	176.98	2.695	2.118
5	2.267	11.88	9.06	0	9.144	113.284	9.144	15.011	10.288	15.011	15.240	83.12	176.98	2.129	1.953
6	2.024	8.12	6.04	5	9.109	113.249	9.144	15.105	10.223	13.417	13.646	82.08	141.39	1.722	1.778
7	1.700	4.94	3.04	10	8.999	113.139	9.144	15.166	10.231	11.836	12.065	82.21	110.03	1.338	1.580

Figure 2.- Details of nozzles. All dimensions are in centimeters except as noted. Areas listed are in square centimeters.

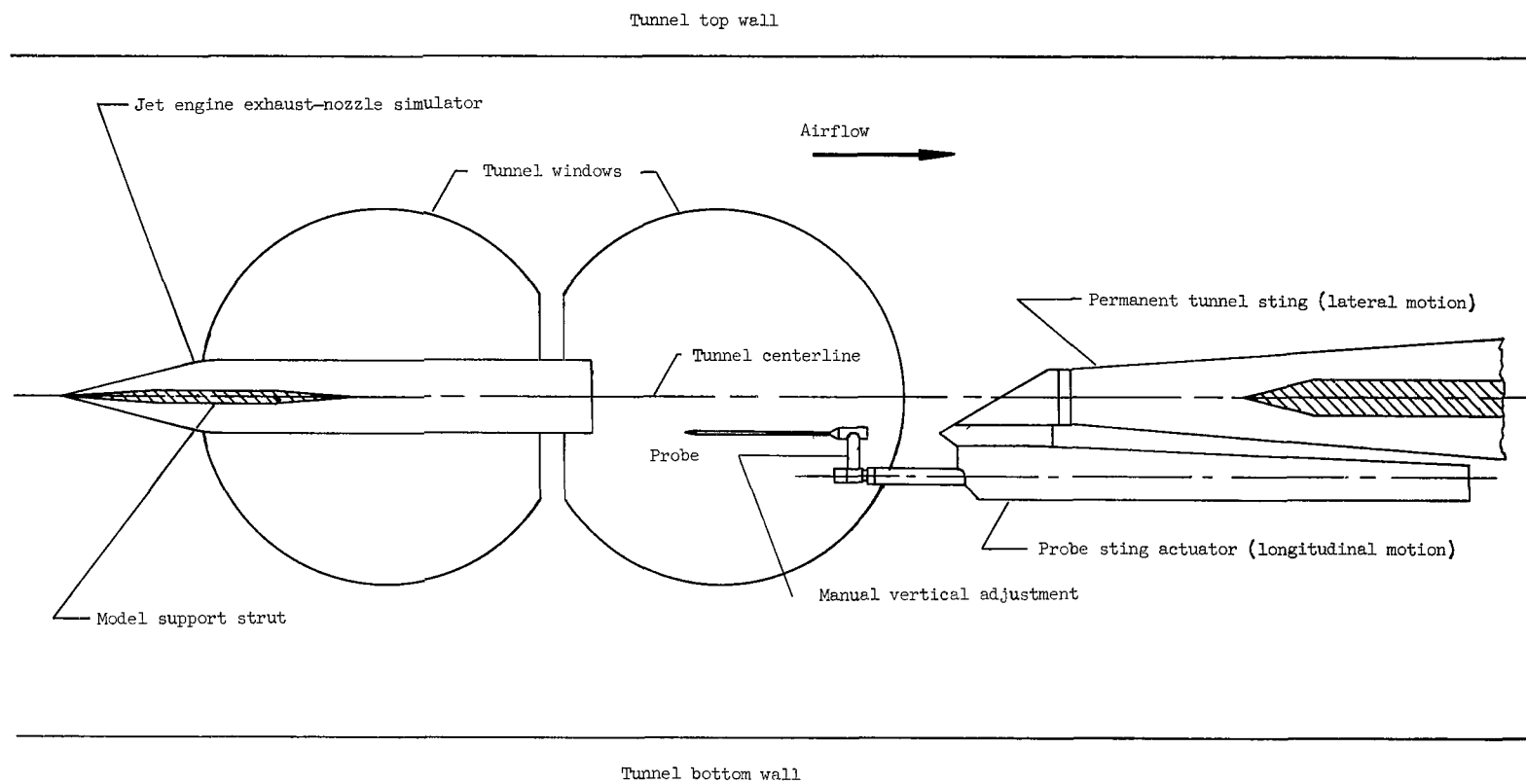
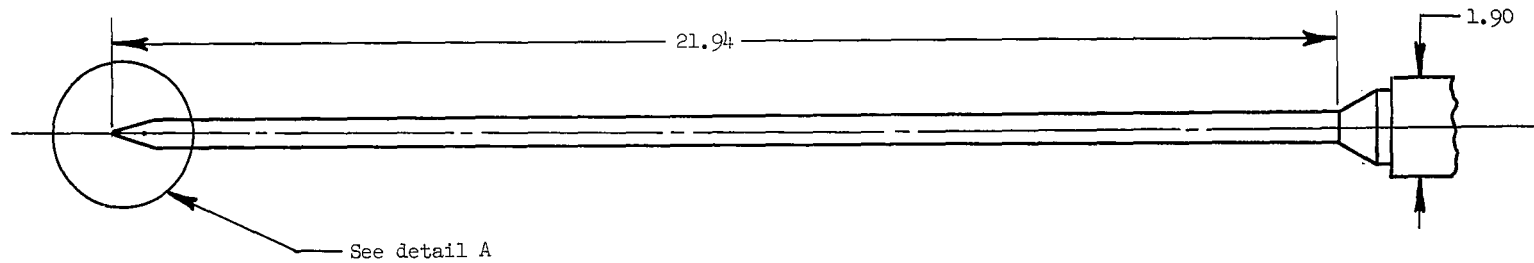
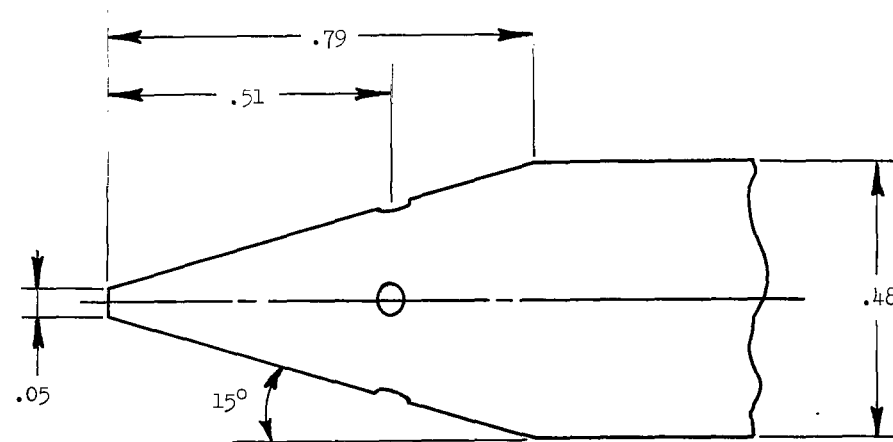


Figure 3.- Wind-tunnel flow-field survey apparatus.



Note: The four 0.05-centimeter-diameter static-pressure orifices on the cone surface are located circumferentially 90° apart.



Detail A

Figure 4.- Sketch of conical probe. All dimensions are in centimeters unless otherwise noted.

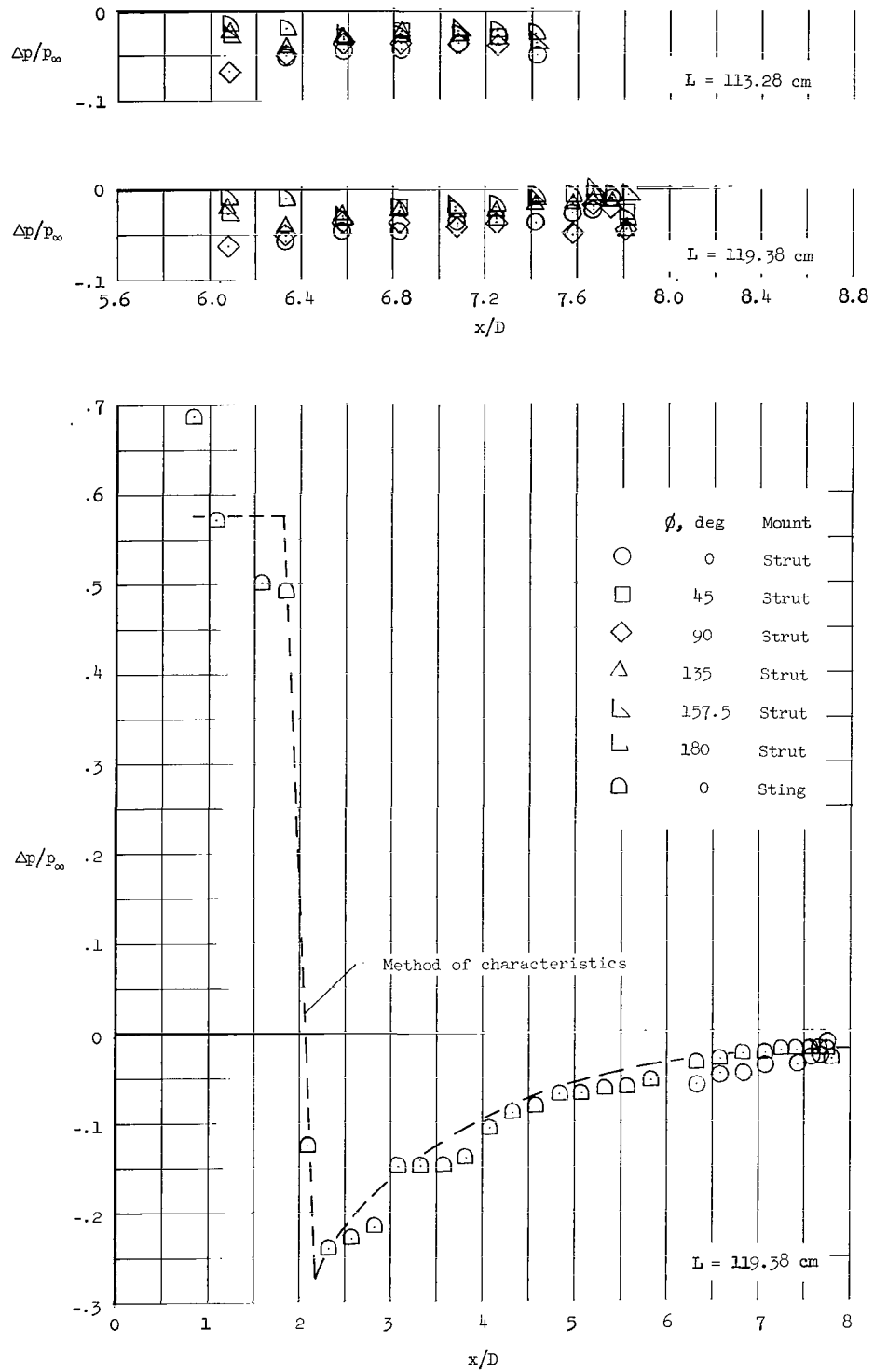
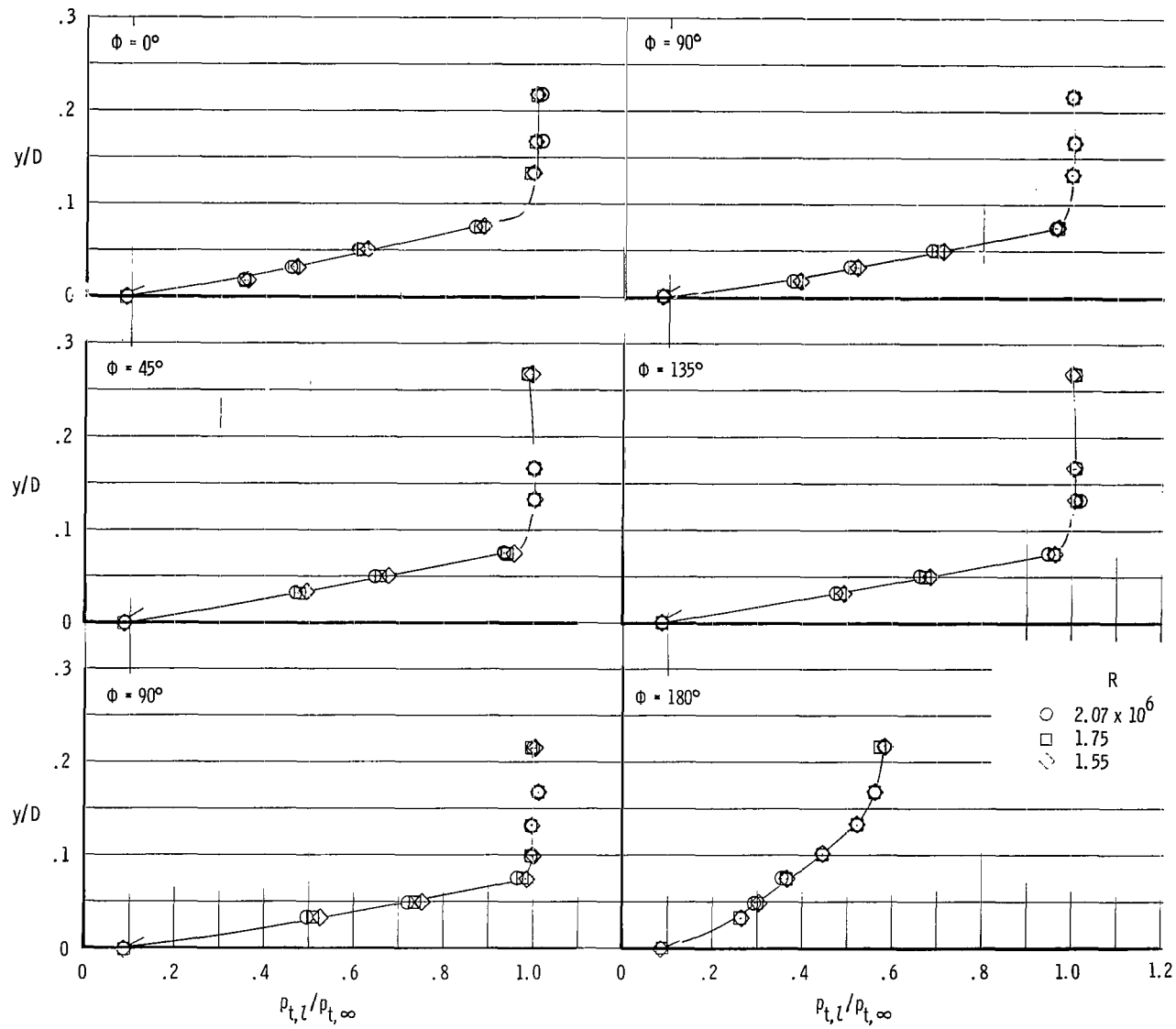
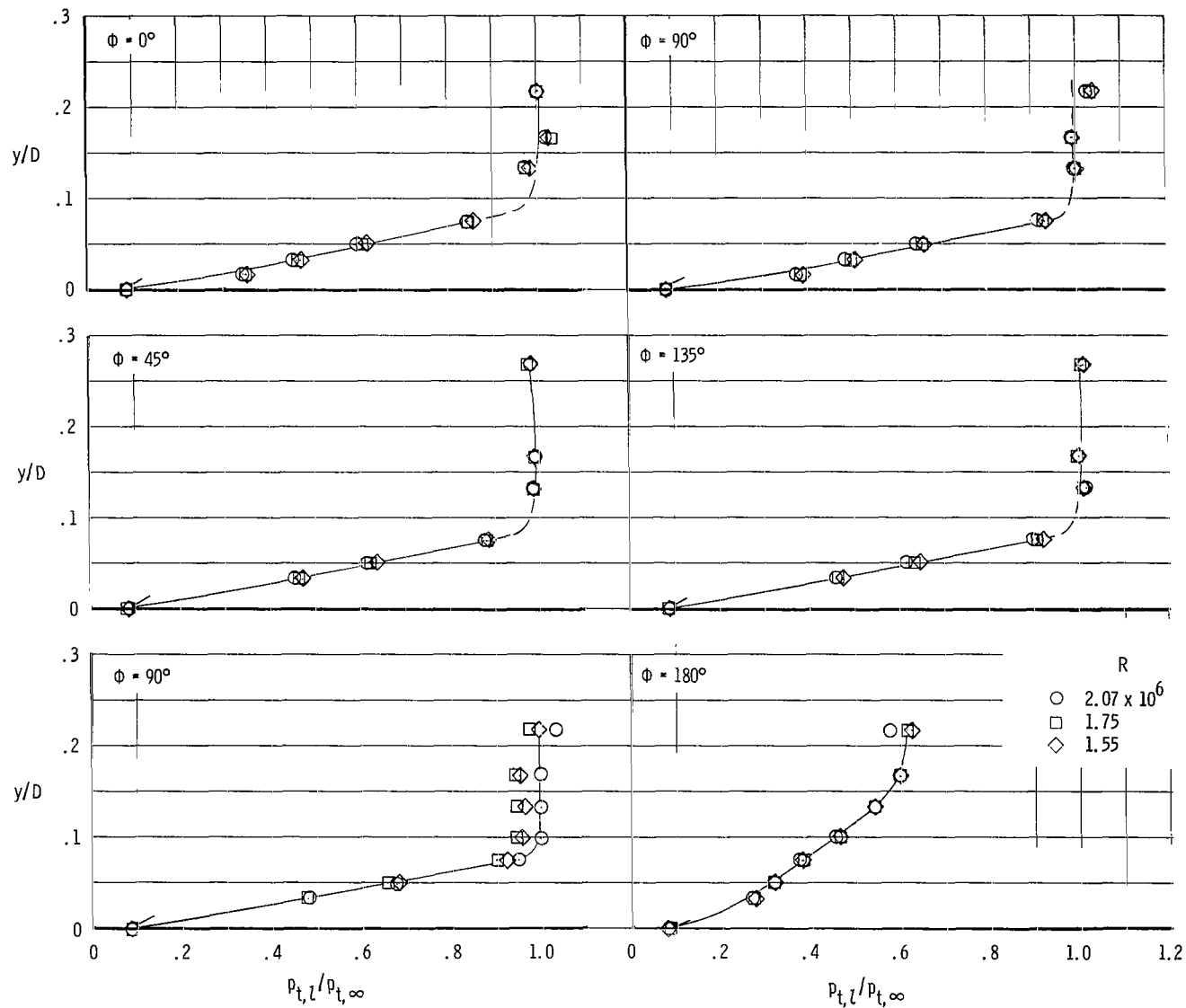


Figure 5.- Surface pressure distribution for jet-exhaust nozzle simulator at $M_\infty = 2.20$, $R = 1.75 \times 10^6$ with transition fixed.



(a) $x/D = 6.833$.

Figure 6.- Boundary-layer stagnation pressure profiles for cylindrical afterbody at two longitudinal positions. $M_\infty = 2.20$.



(b) $x/D = 7.200$.

Figure 6.- Concluded.

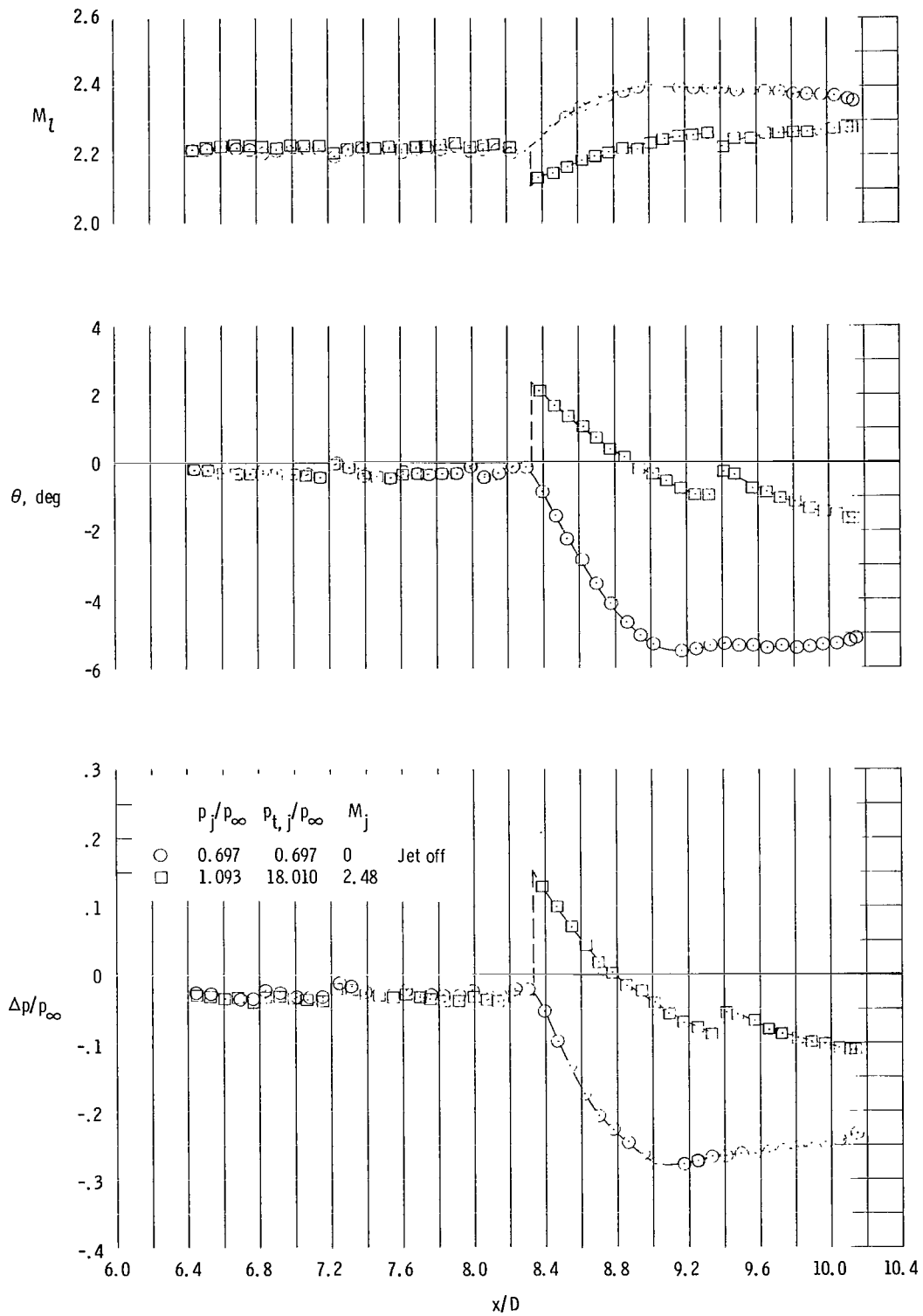


Figure 7.- Flow-field interference signatures for nozzle 4 obtained during phase I. $M_\infty = 2.20$; $z/D = 1.00$.

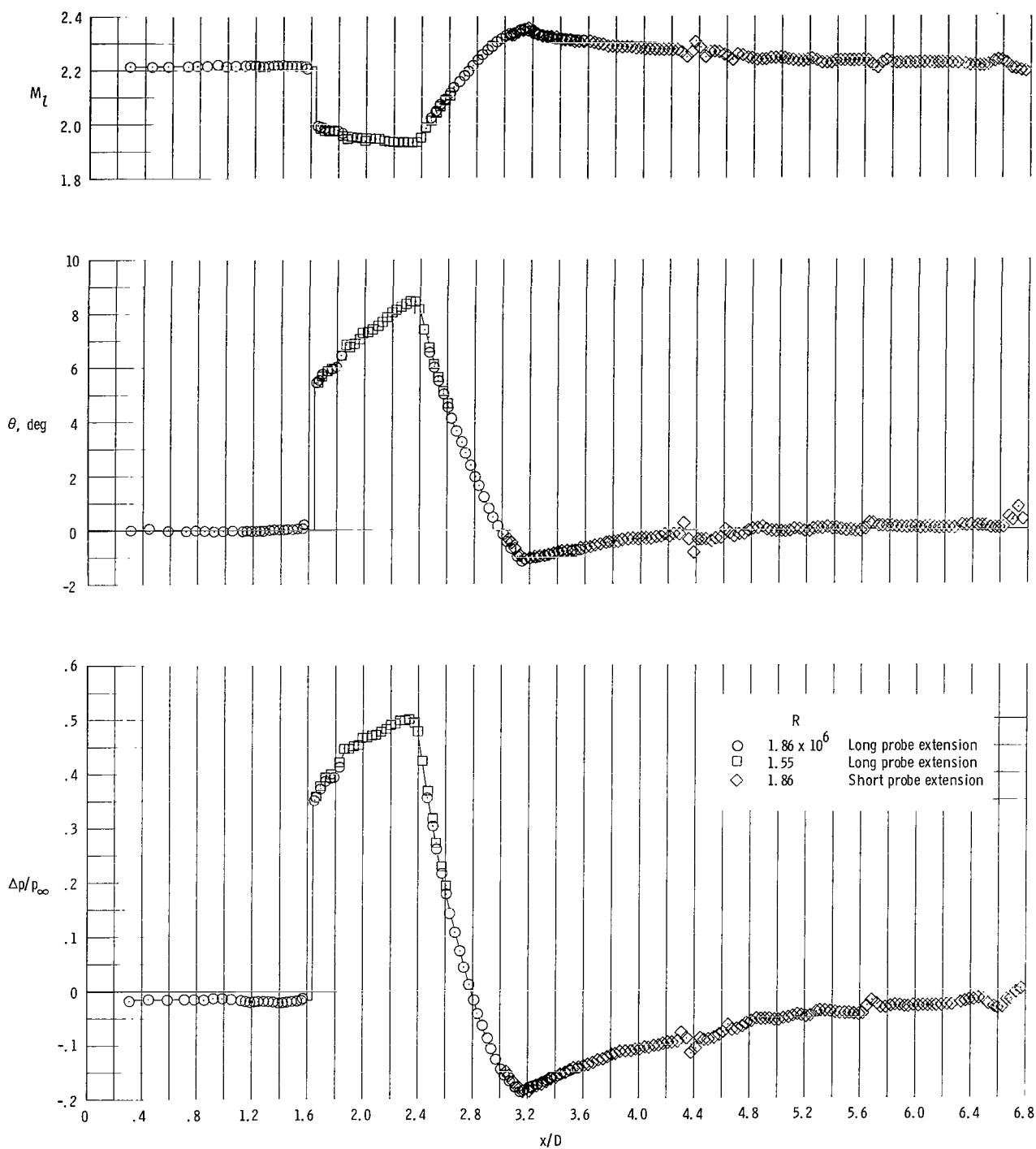
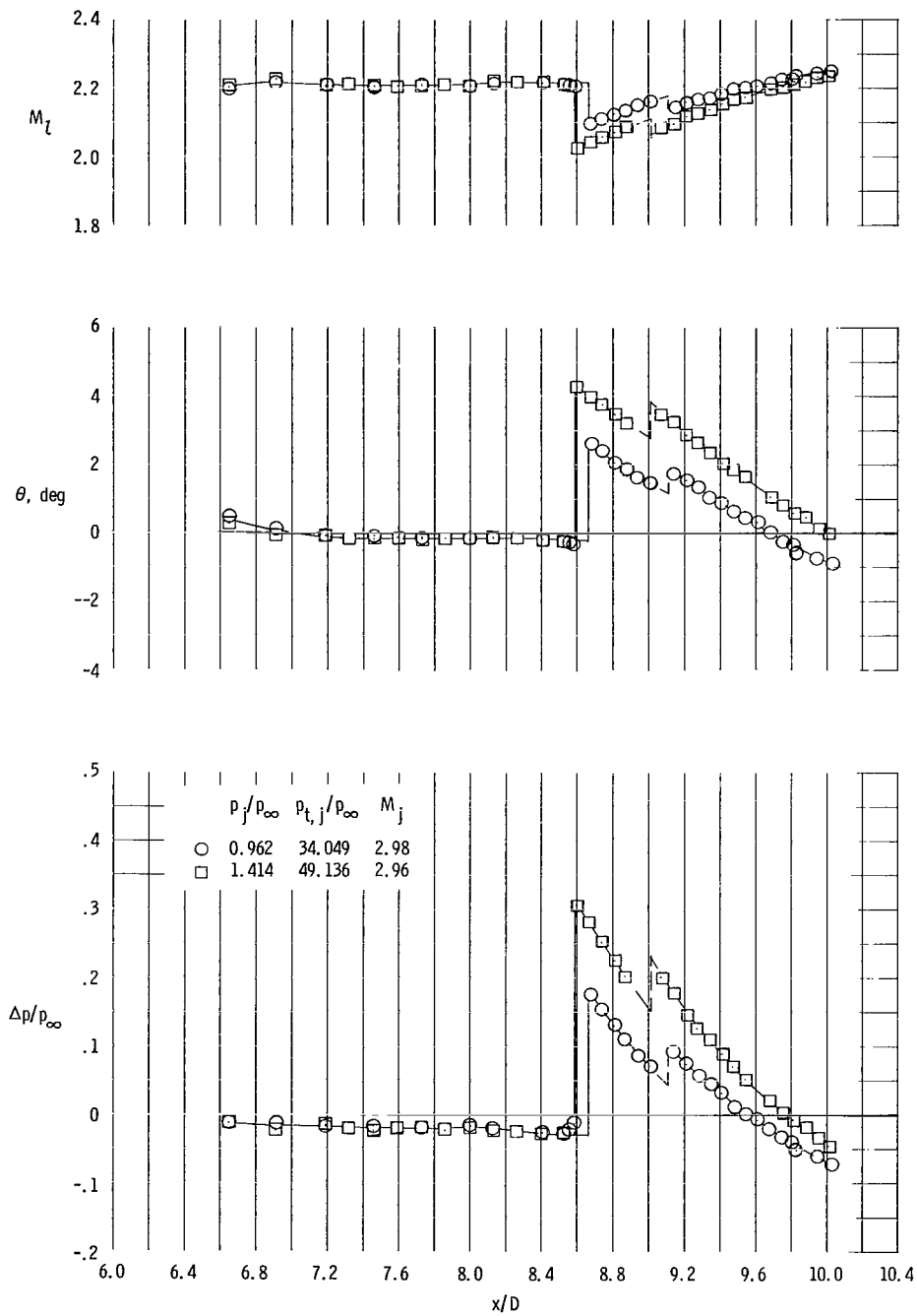
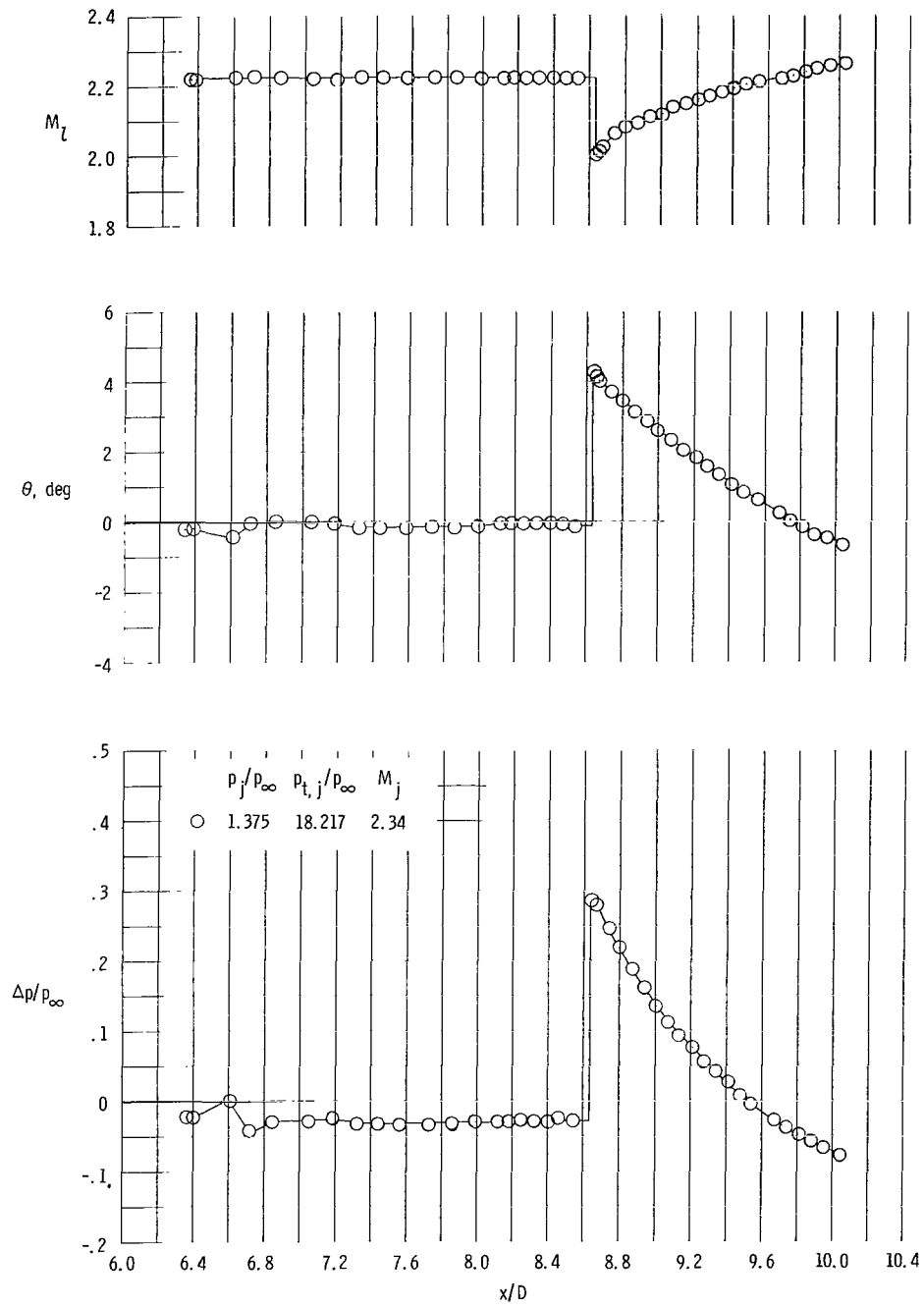


Figure 8.- Flow-field signatures for 14° cone-cylinder forebody of jet-engine exhaust-nozzle simulator obtained during phase II.
 $M_\infty = 2.20$; $z/D = 1.00$.



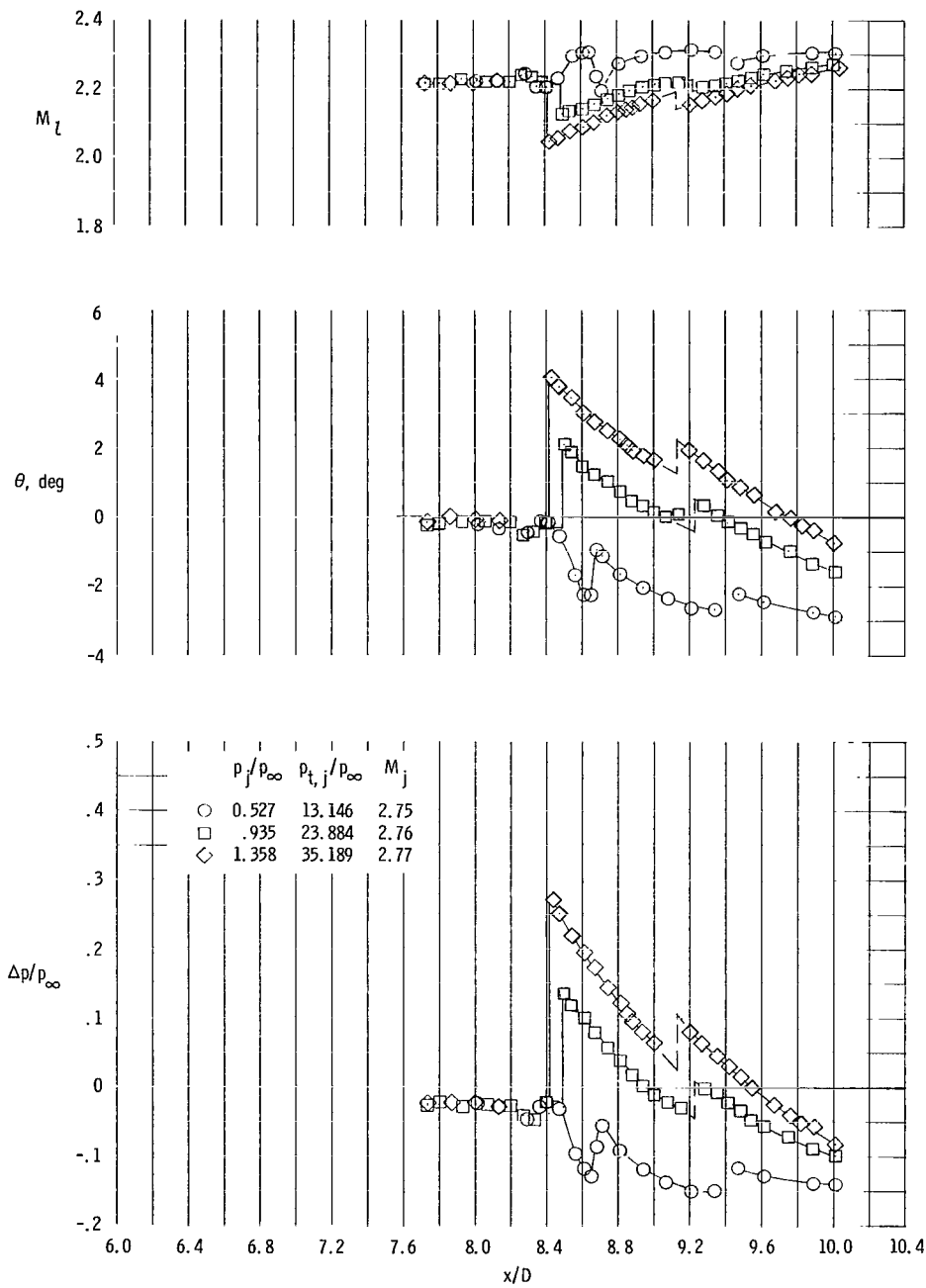
(a) Nozzle 1.

Figure 9.- Flow-field interference signatures for various nozzles tested during phase II. $M_\infty = 2.20$; $z/D = 1.00$.



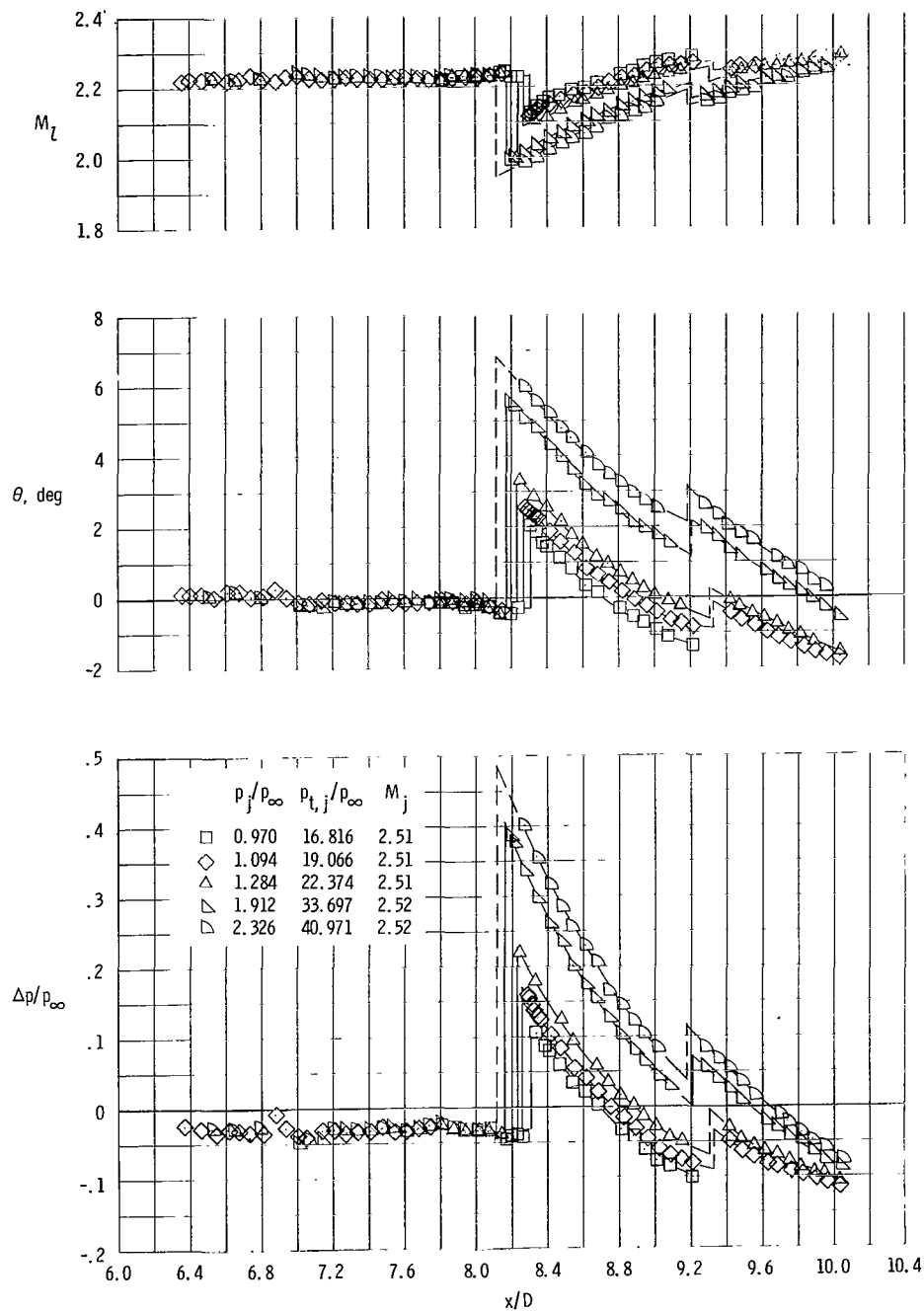
(b) Nozzle 2.

Figure 9.- Continued.



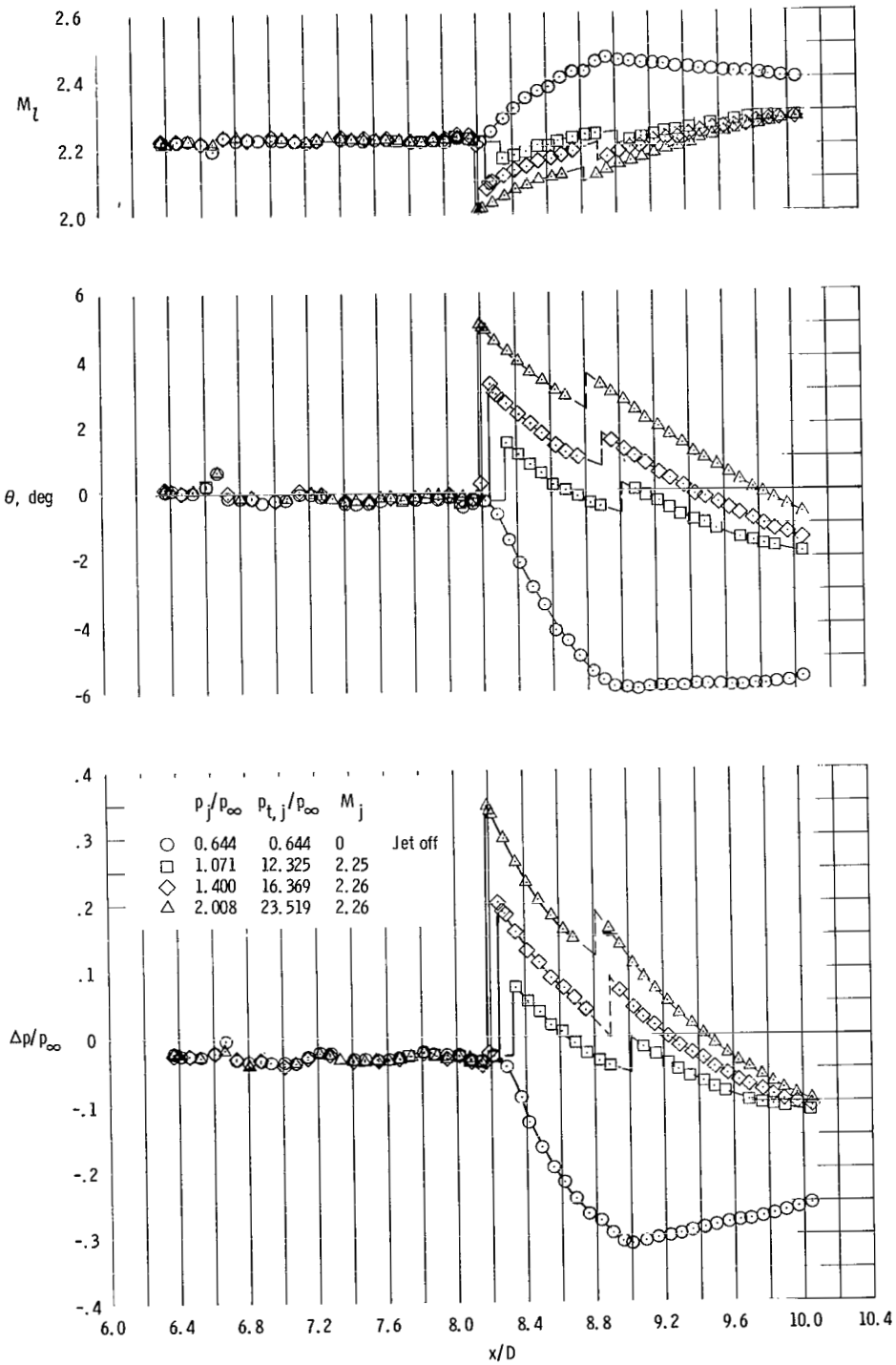
(c) Nozzle 3.

Figure 9.- Continued.



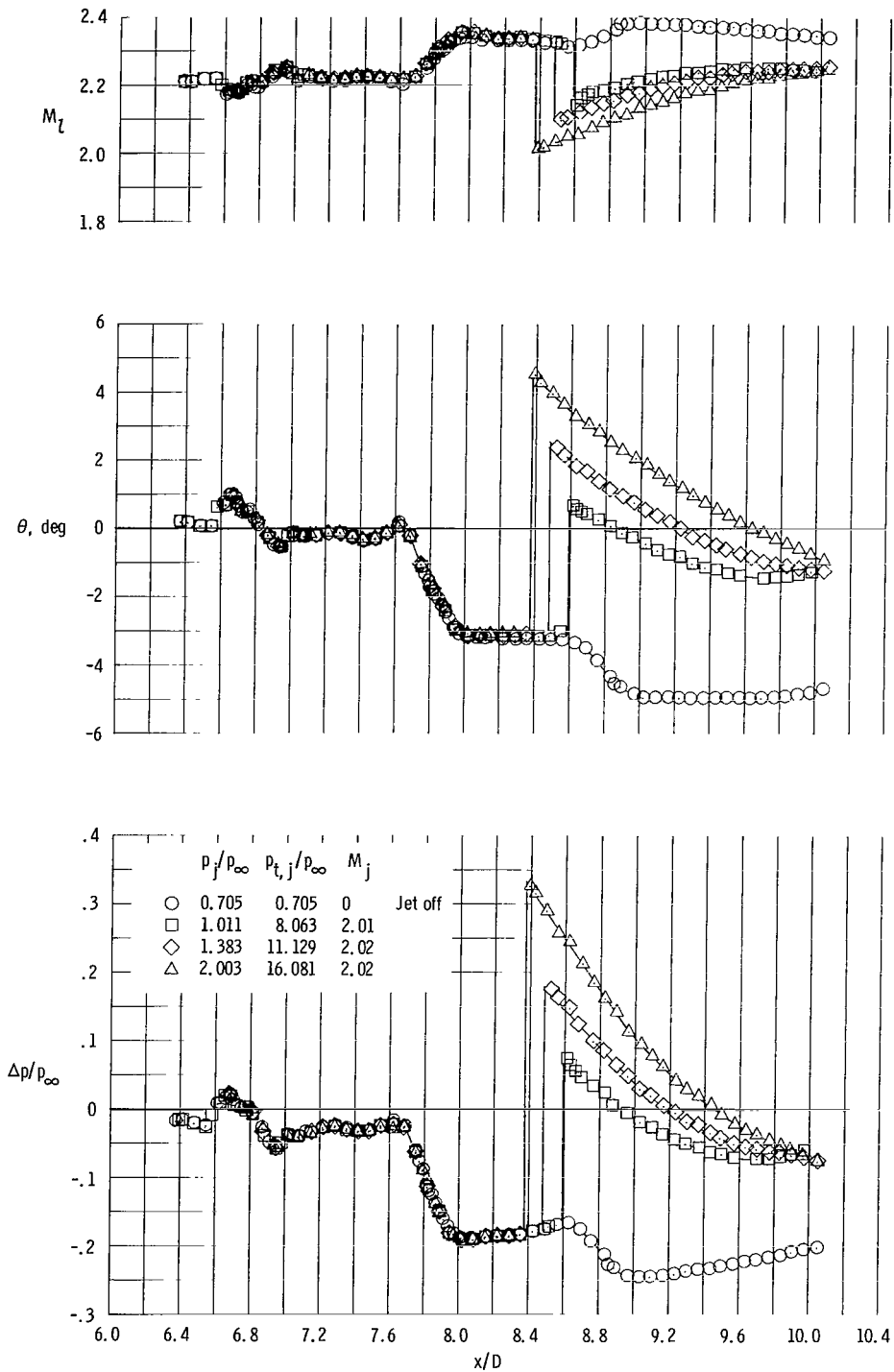
(d) Nozzle 4.

Figure 9.- Continued.



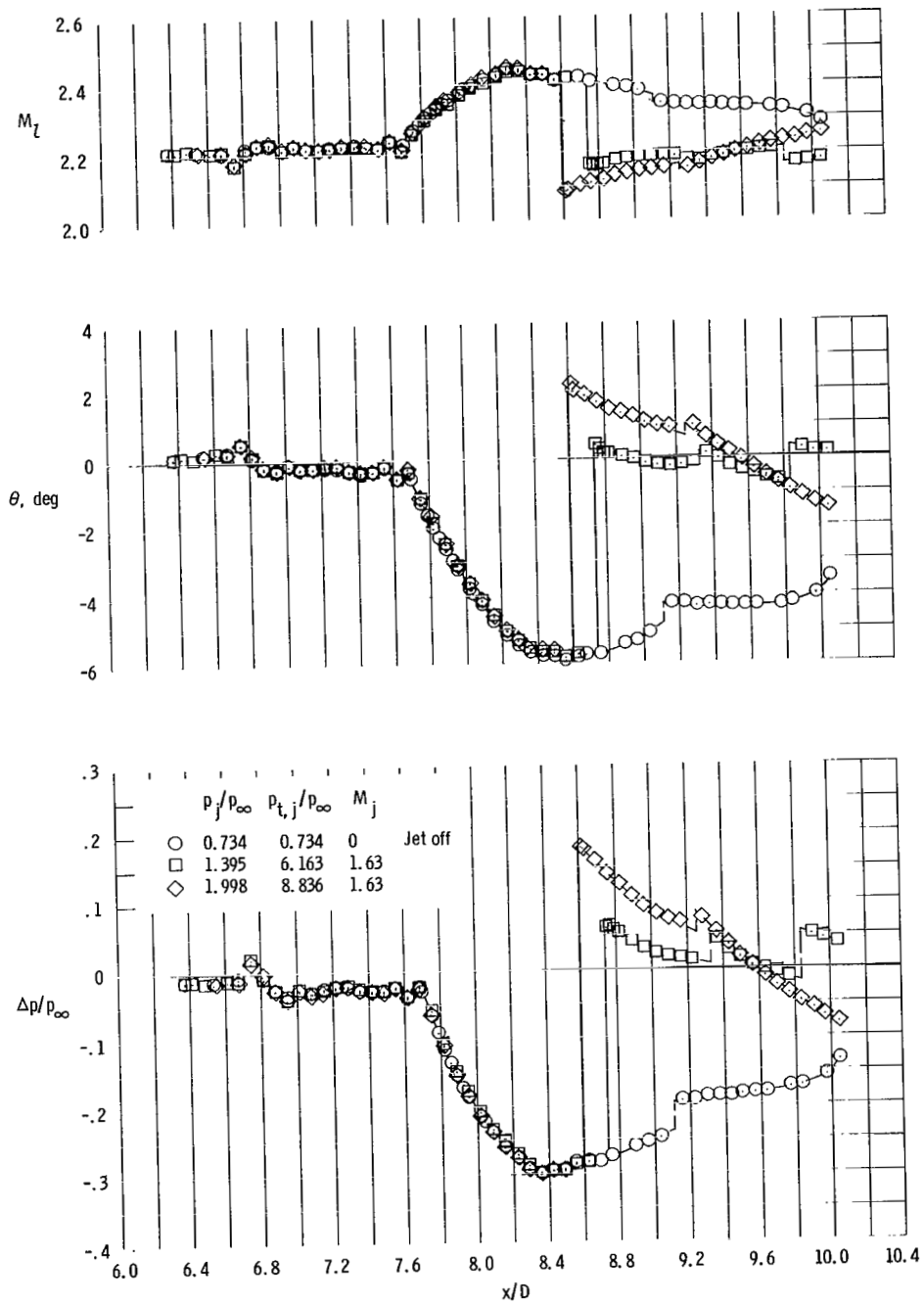
(e) Nozzle 5.

Figure 9.- Continued.



(f) Nozzle 6.

Figure 9.- Continued.



(g) Nozzle 7.

Figure 9.- Concluded.

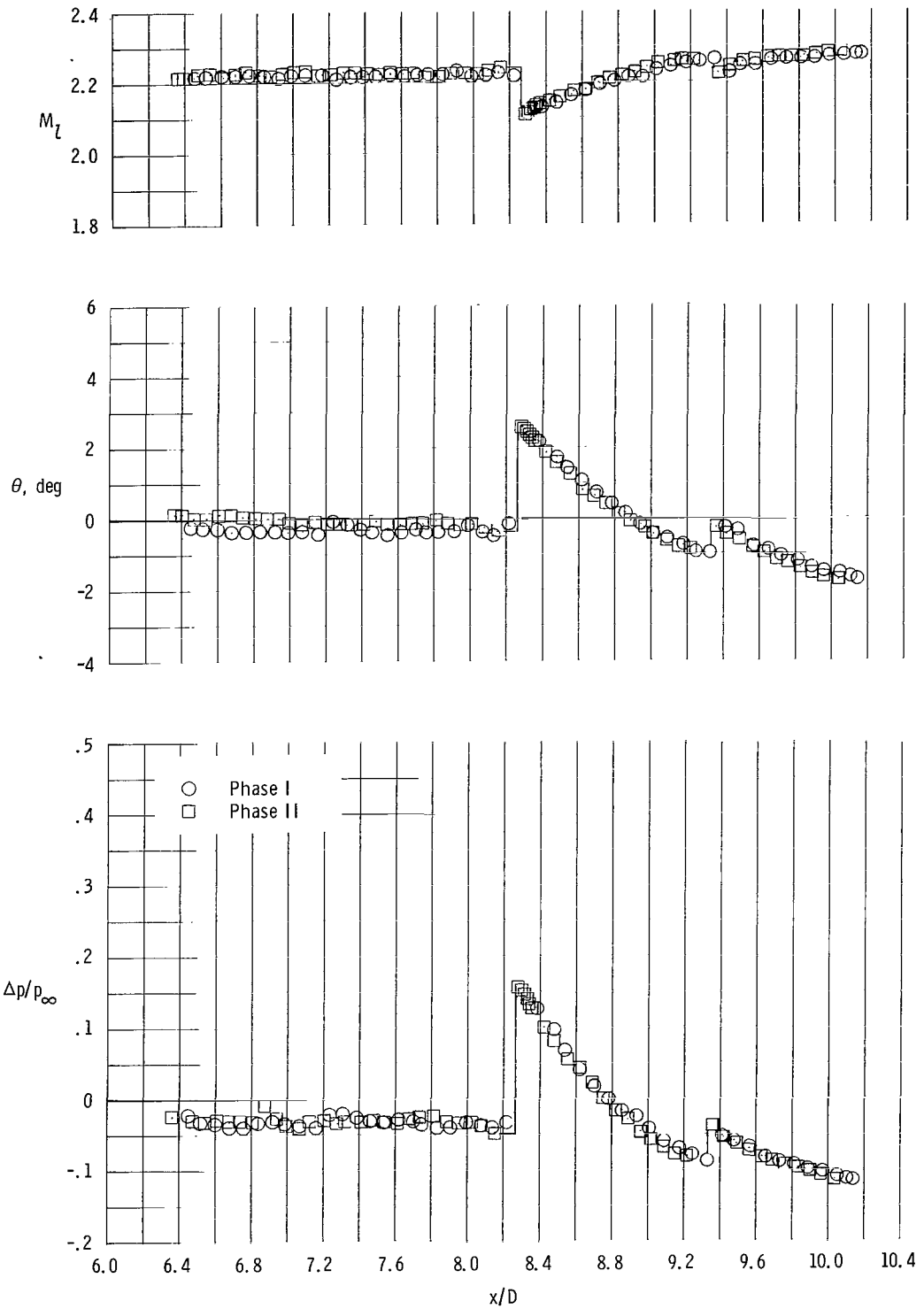


Figure 10.- Comparison of phase I and phase II flow-field interference signatures for nozzle 4 with jet exhausting at $p_j/p_\infty \approx 1.09$, $M_\infty = 2.20$; $z/D = 1.00$.

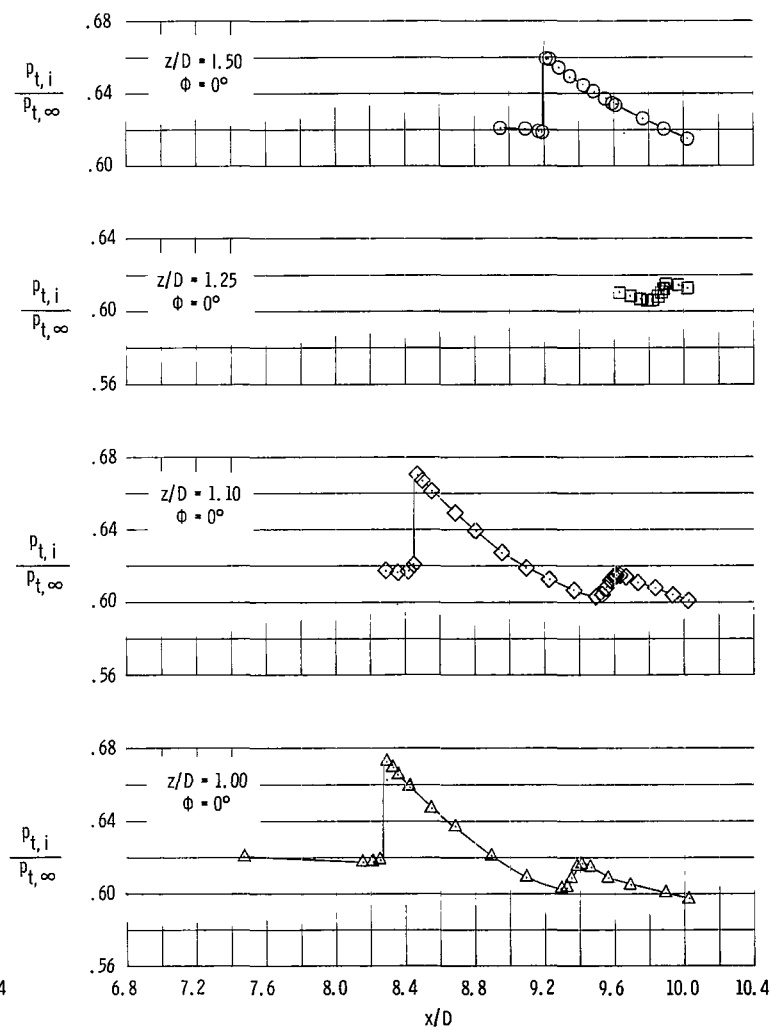
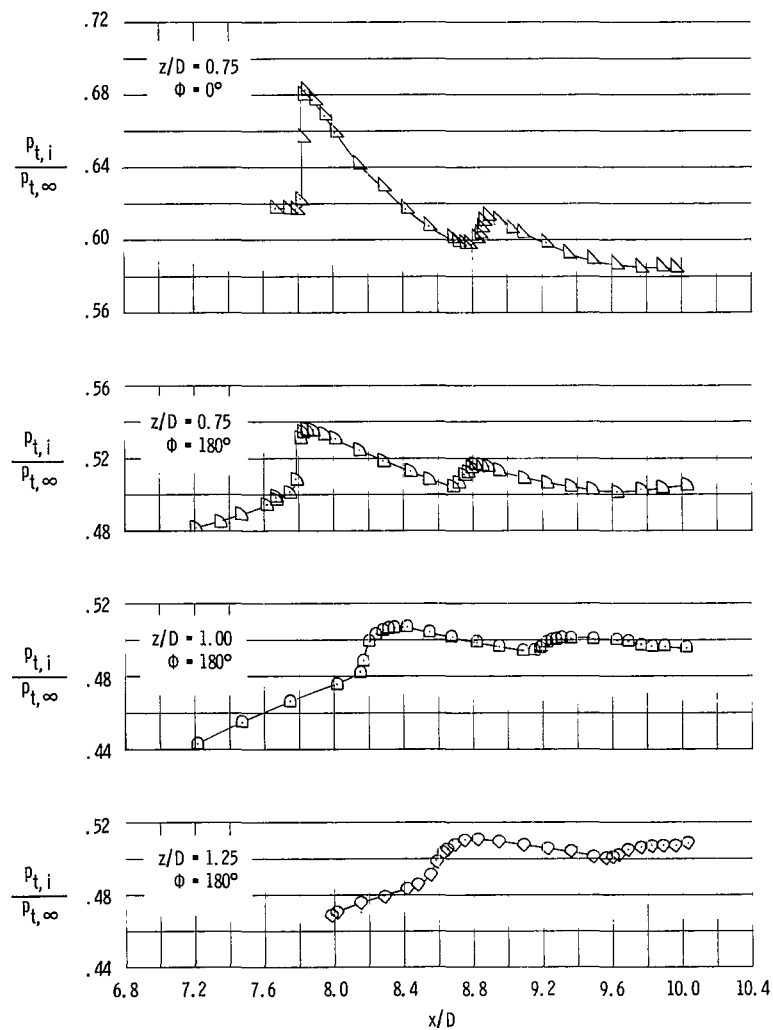


Figure 11.- Flow-field measurements of ratio of probe impact pressure to free-stream stagnation pressure for nozzle 4. $p_j/p_\infty = 1.094$; $M_\infty = 2.20$.

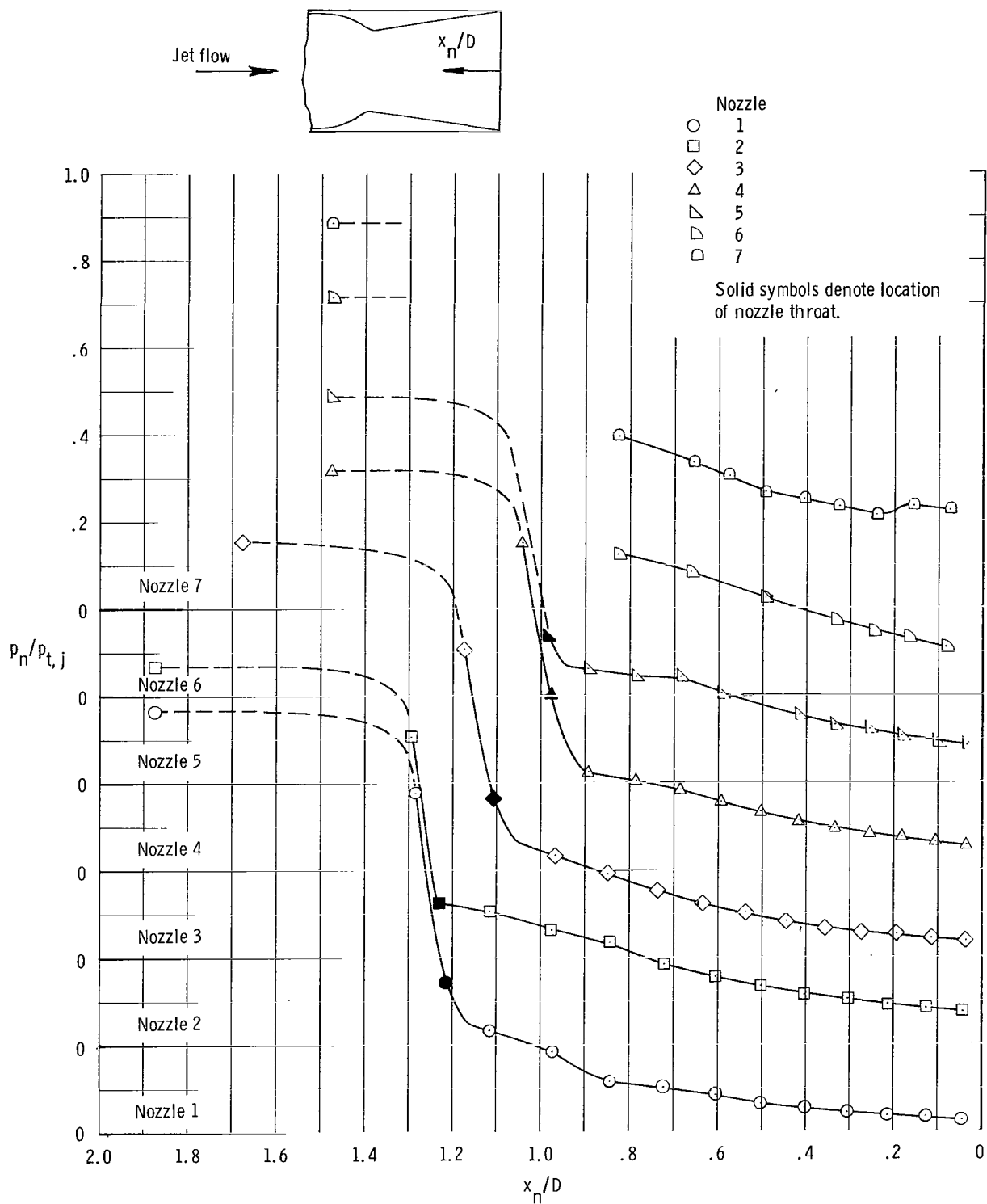
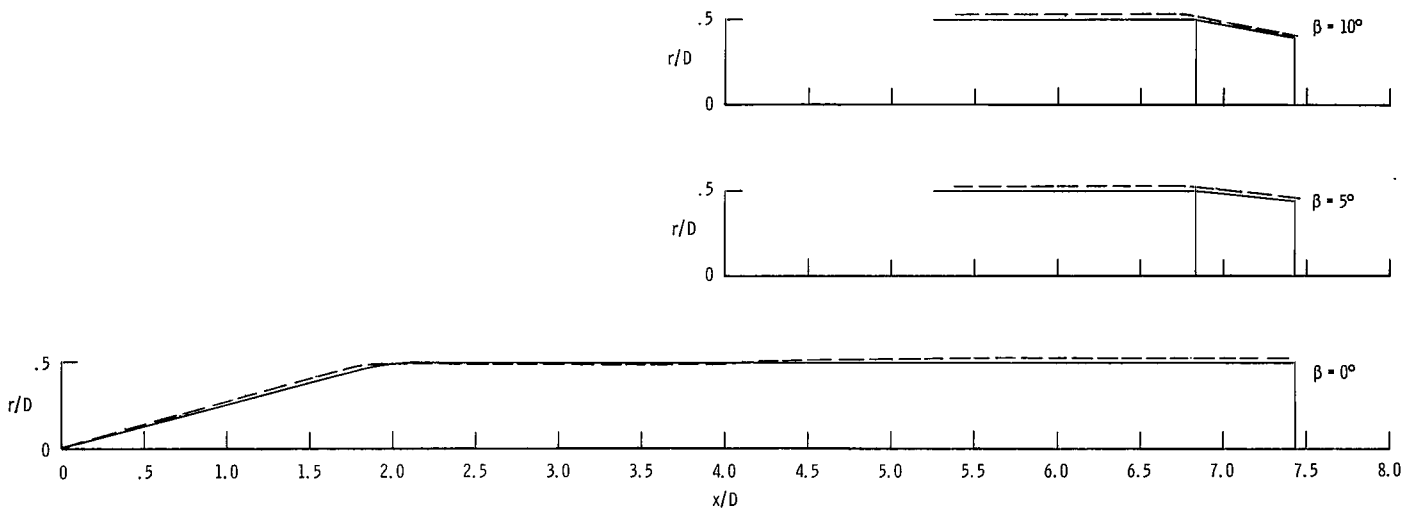
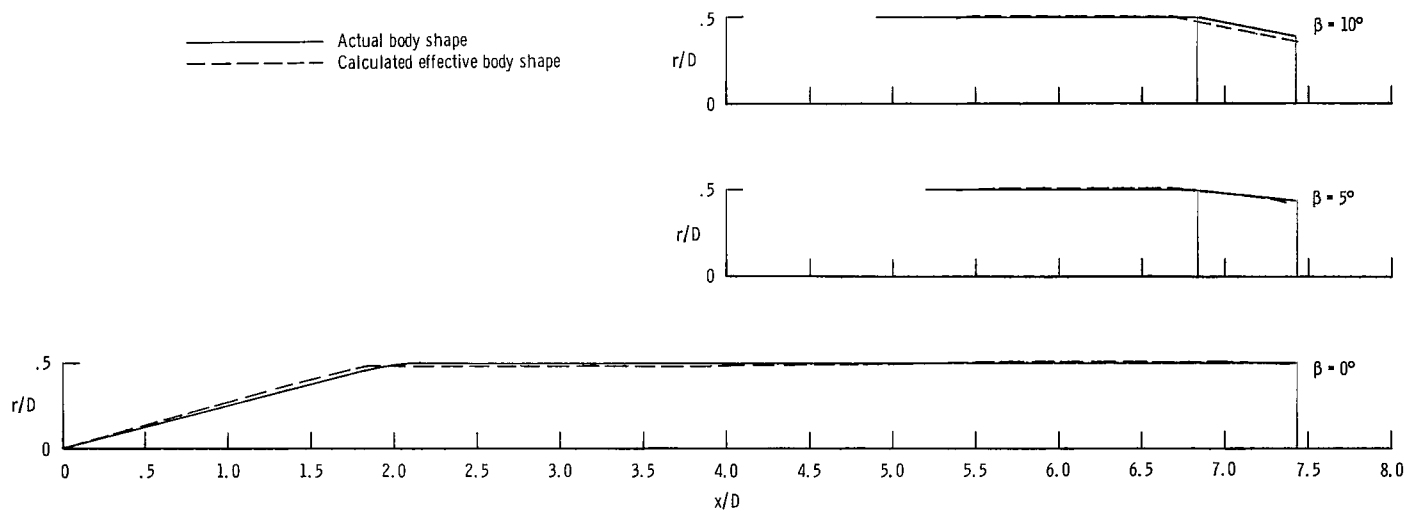


Figure 12.- Variation of static pressure along wall of each nozzle. Data presented are average values for all jet-on operating conditions for each nozzle, $M_\infty = 2.20$.



(a) Calculated effective body shapes not corrected for boundary-layer displacement effects.



(b) Calculated effective body shapes corrected for boundary-layer displacement effects.

Figure 13.- Comparison of calculated effective body shapes with actual body shapes of jet-engine simulator with various boattail afterbodies.

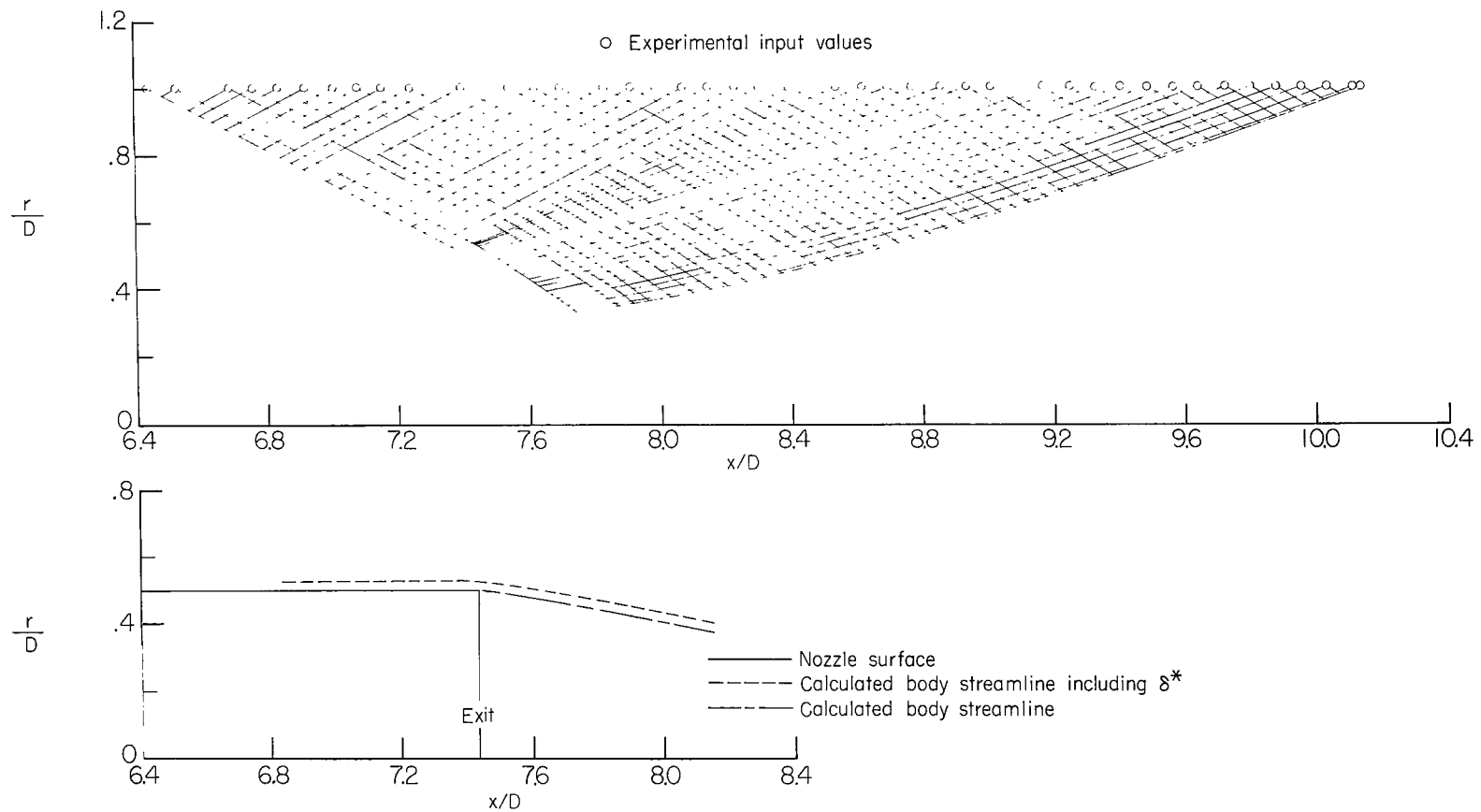


Figure 14.- Equivalent solid body shape and characteristic net for nozzle 4 with jet off. $M_\infty = 2.20$; phase I. (Three iterations used to calculate characteristic net.)

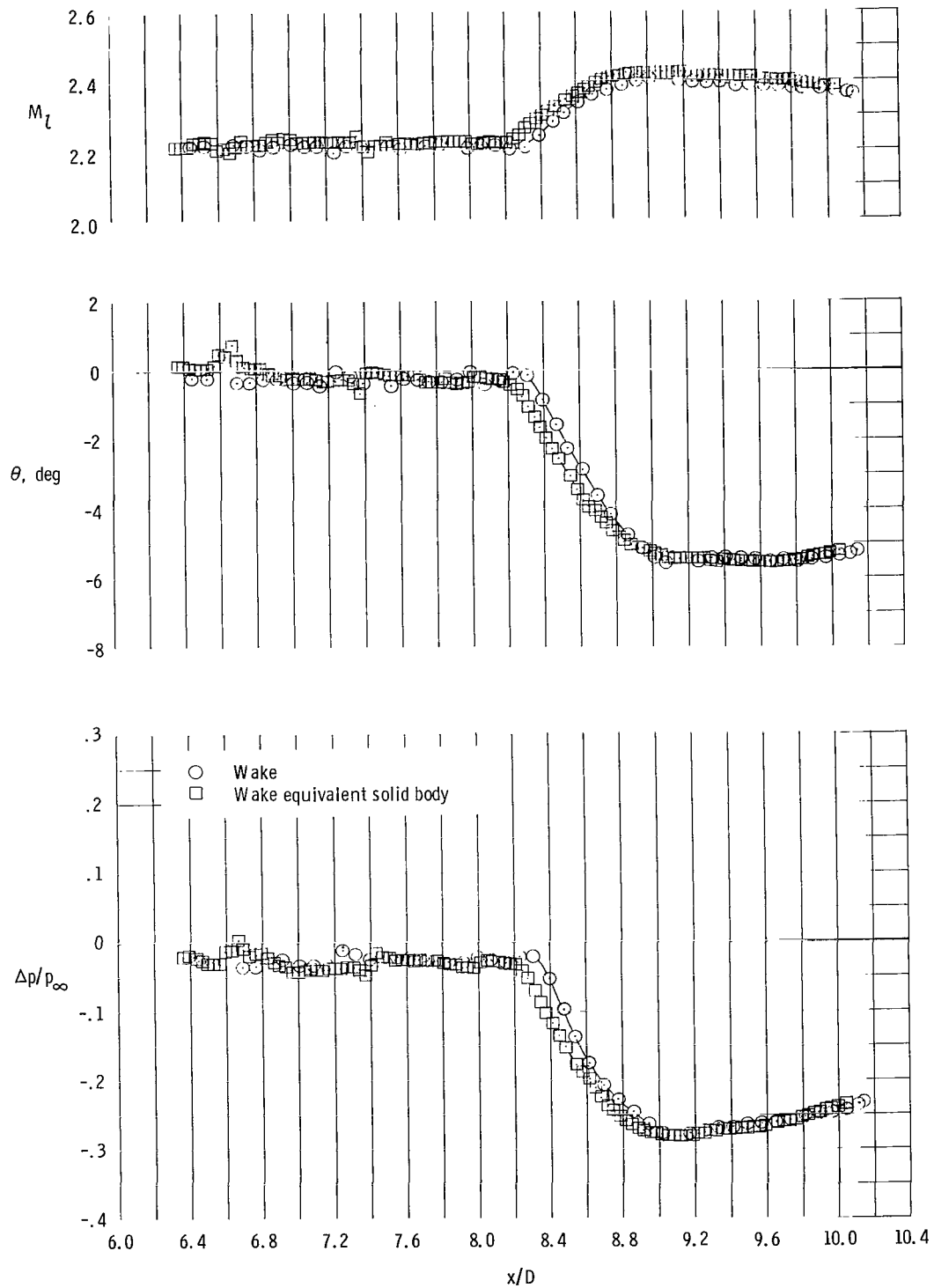


Figure 15.- Comparison of flow-field interference signatures of nozzle 4, jet off (phase I), with corresponding equivalent solid body.
 $M_\infty = 2.20$; $z/D = 1.00$.

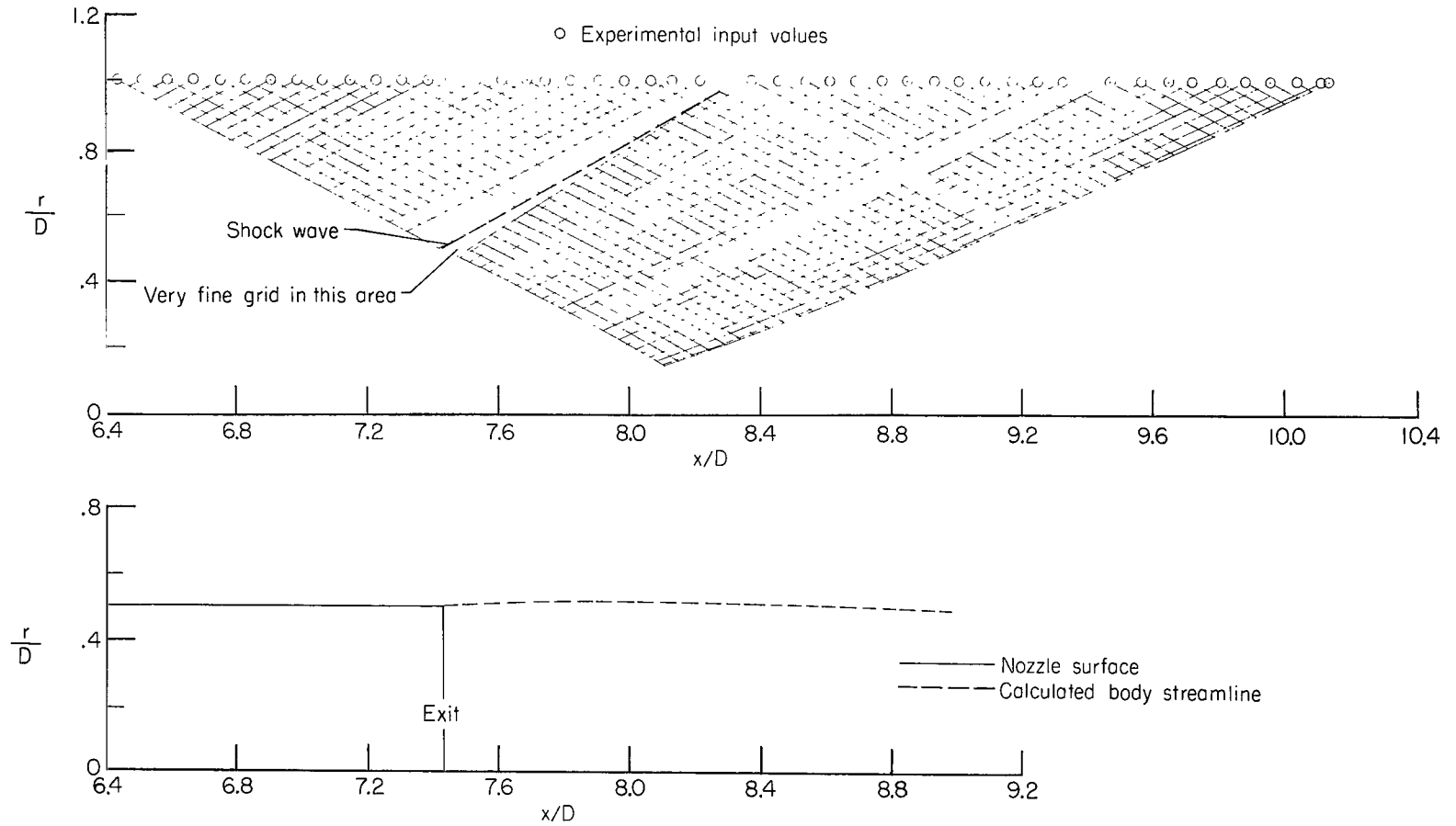


Figure 16.- Equivalent solid body shape and characteristic net for nozzle 4 with jet on. $p_i/p_\infty = 1.093$; $M_\infty = 2.20$; phase I. (Three iterations used to calculate characteristic net.)

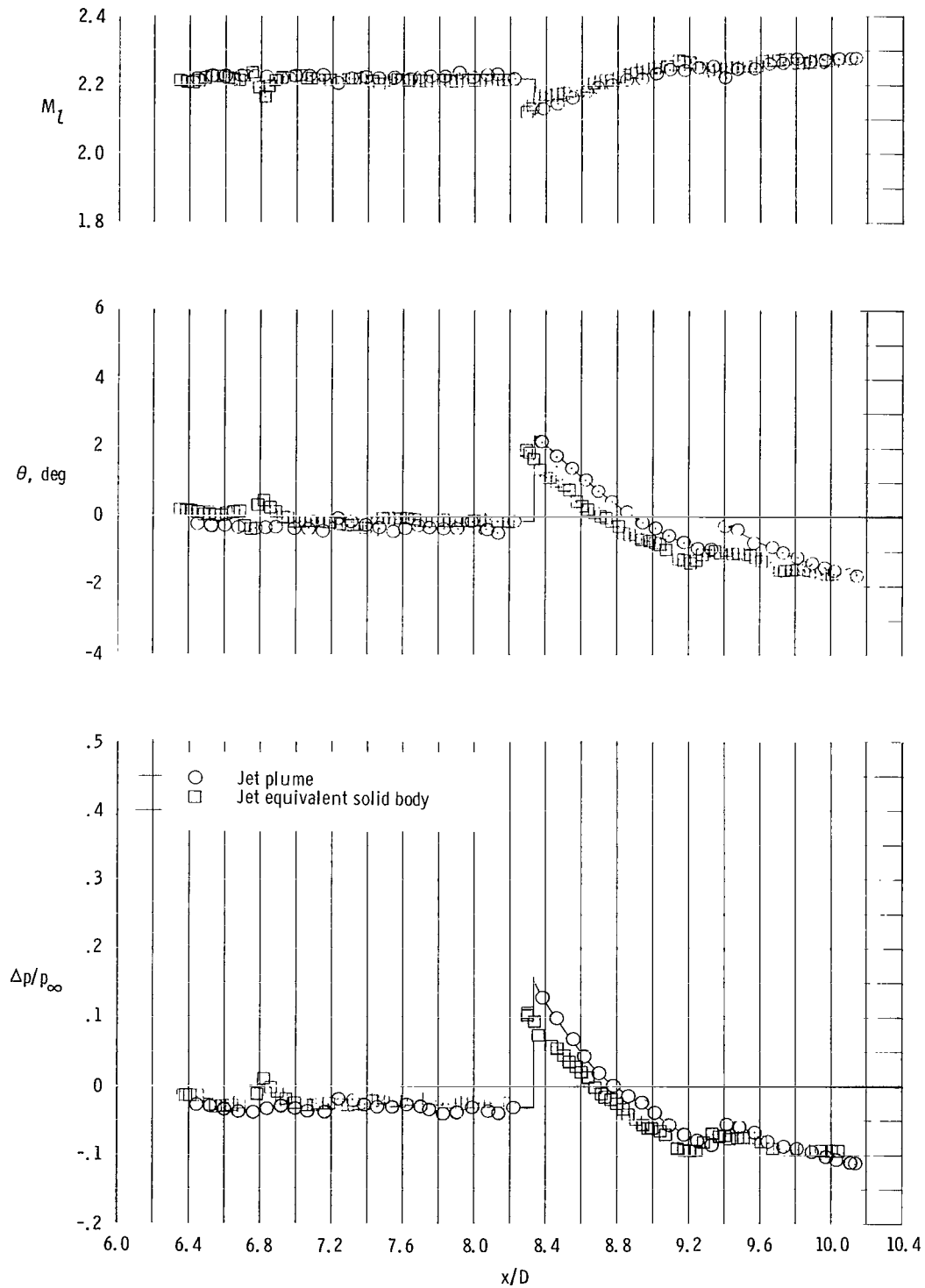
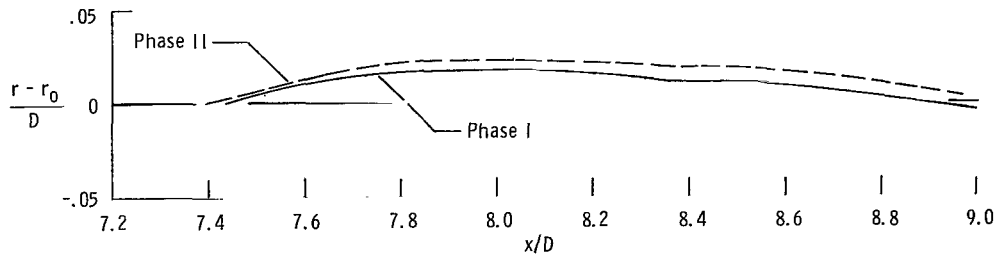
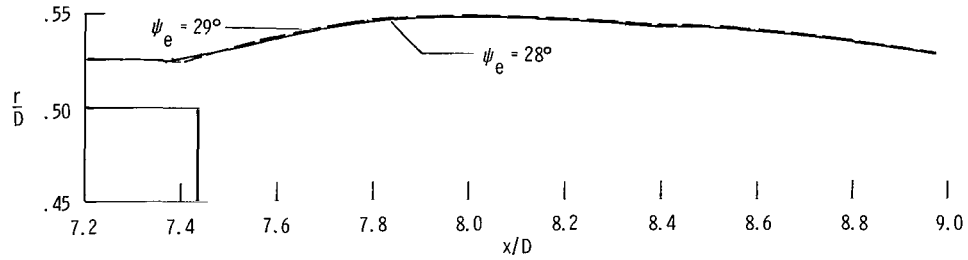


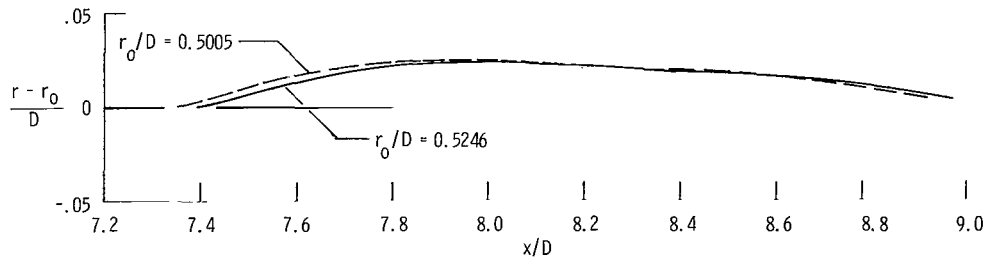
Figure 17.- Comparison of flow-field interference signatures of nozzle 4, jet exhausting at $p_i/p_\infty = 1.093$ (phase I), with corresponding equivalent solid body. $M_\infty = 2.20$; $z/D = 1.00$.



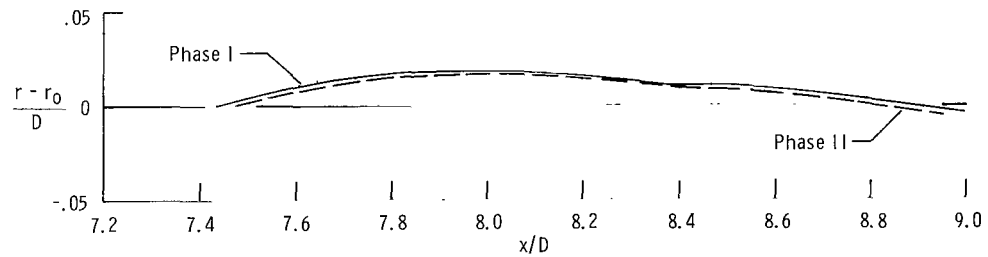
(a) Comparison of jet effective solid bodies calculated from Phase I and II data.



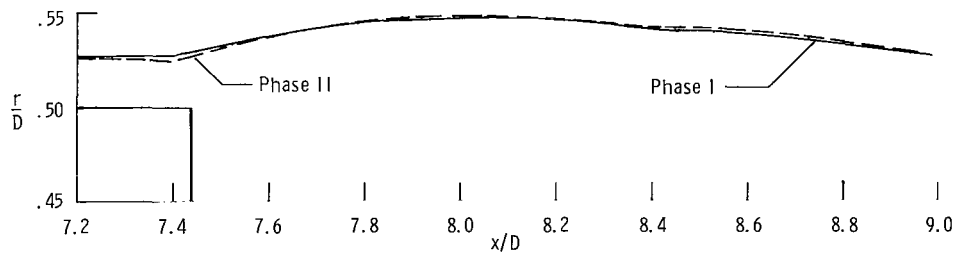
(b) Effect of exit shock angle on calculated jet effective solid body shape (Phase II data).



(c) Effect of including boundary layer displacement thickness in the initial streamline radius (Phase II data).

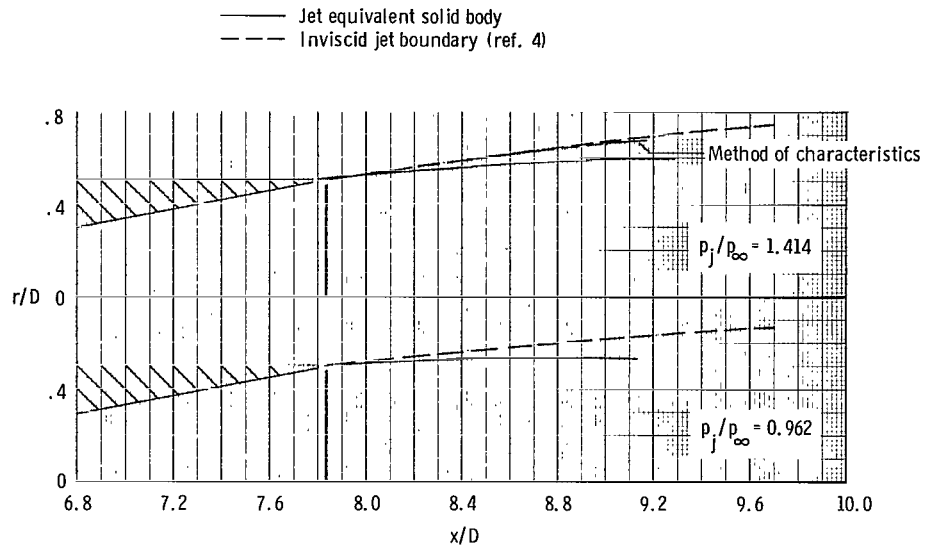


(d) Comparison of jet effective solid bodies calculated from Phase I and II data using the Phase I exit shock angle and location.

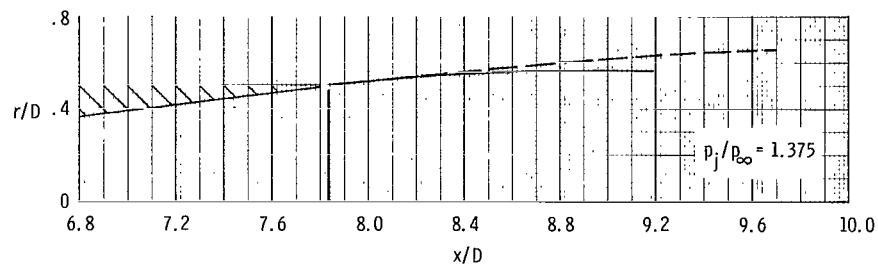


(e) Comparison of jet effective solid bodies calculated from phase I and phase II data using phase II exit shock angle and location.

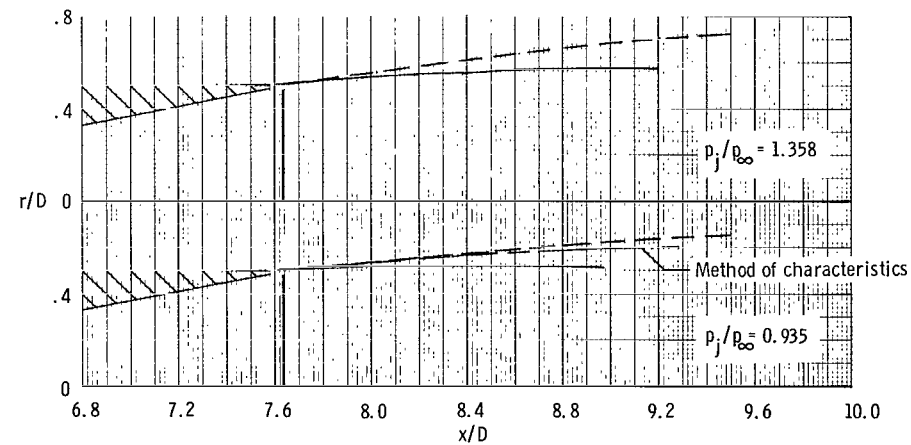
Figure 18.- Effect of various parameters on calculated jet effective solid body shape of a jet exhausting from nozzle 4 at $p_j/p_\infty = 1.094$.



(a) Nozzle 1.

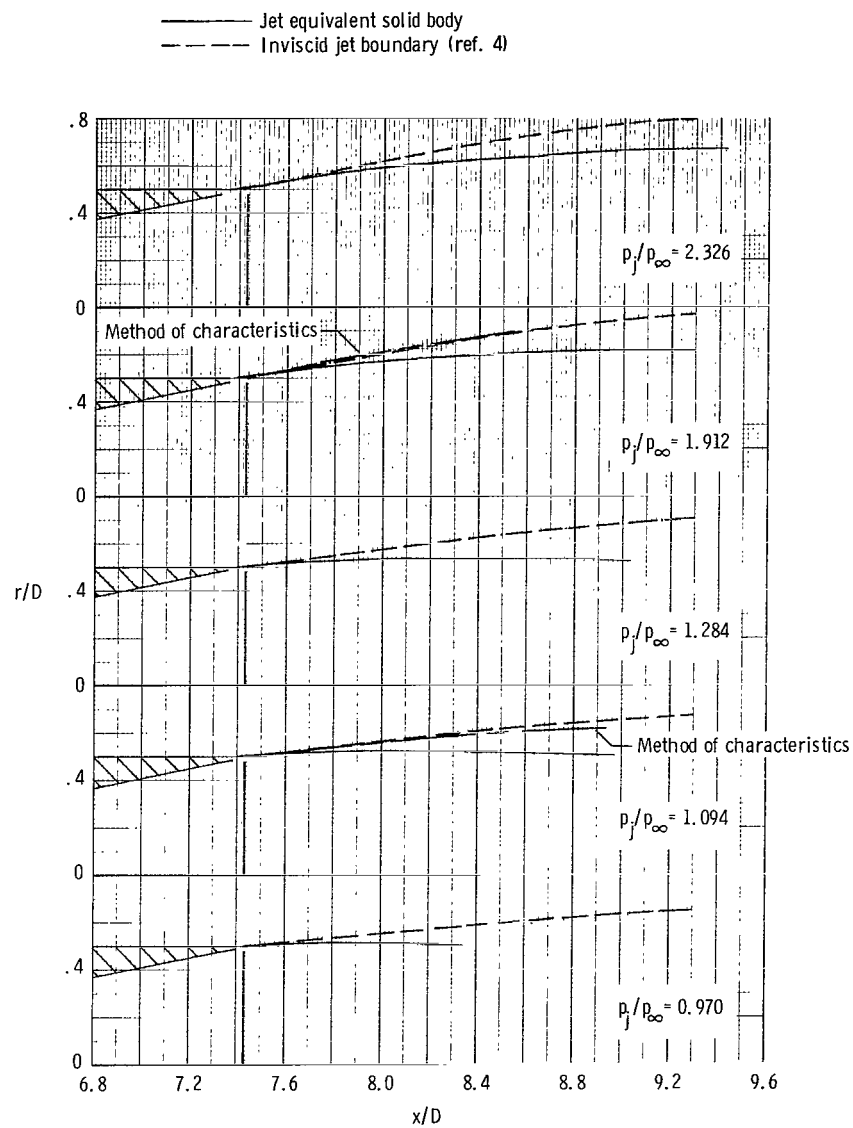


(b) Nozzle 2.



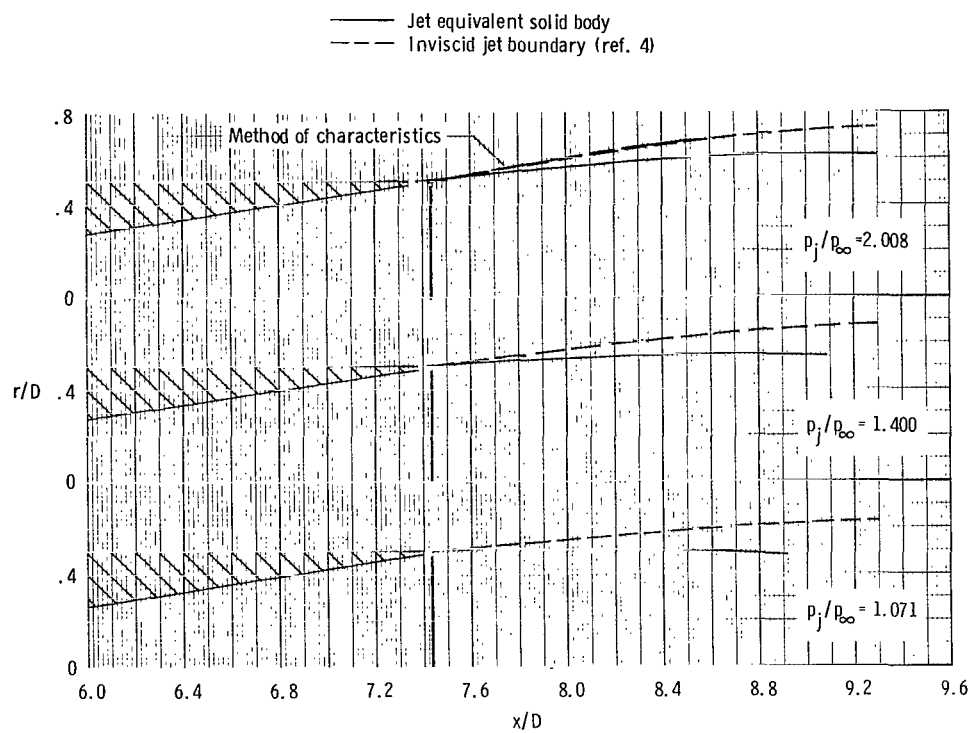
(c) Nozzle 3.

Figure 19.- Comparison of jet equivalent solid body with inviscid jet boundary for jets exhausting from various nozzles at several jet static-pressure ratios.



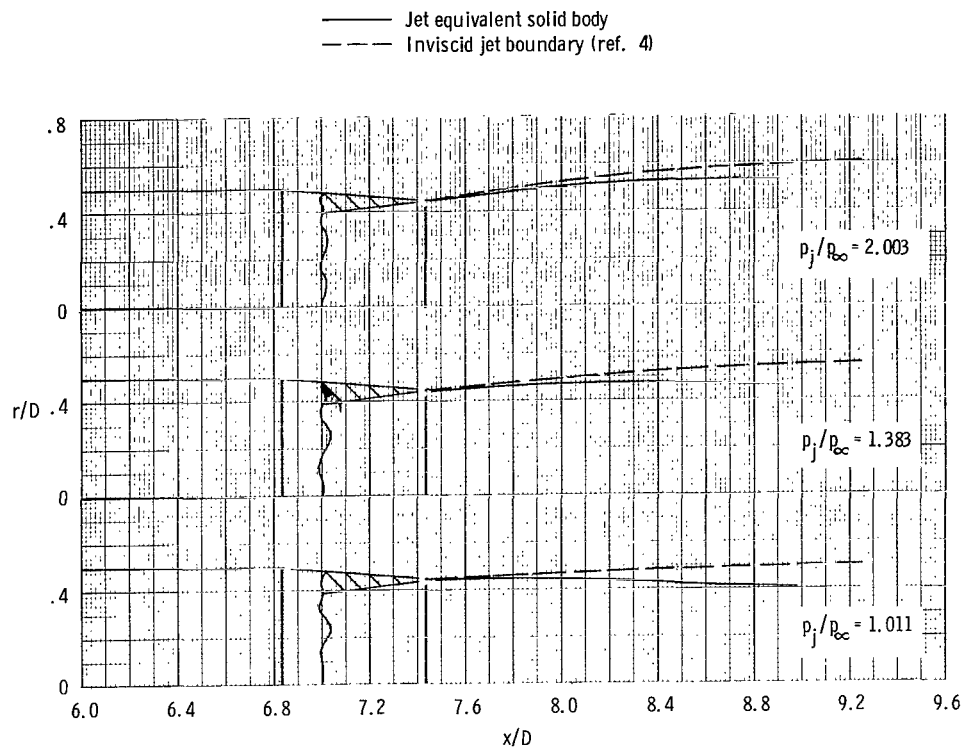
(d) Nozzle 4.

Figure 19.- Continued.

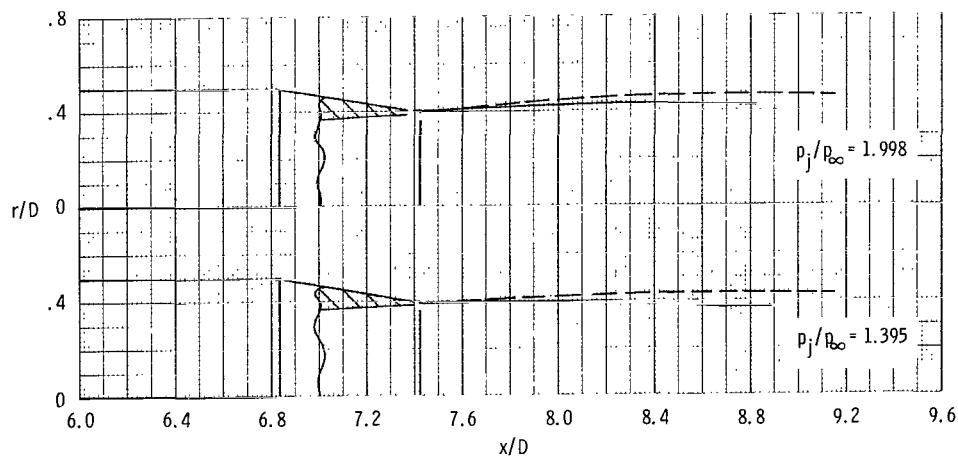


(e) Nozzle 5.

Figure 19.- Continued.

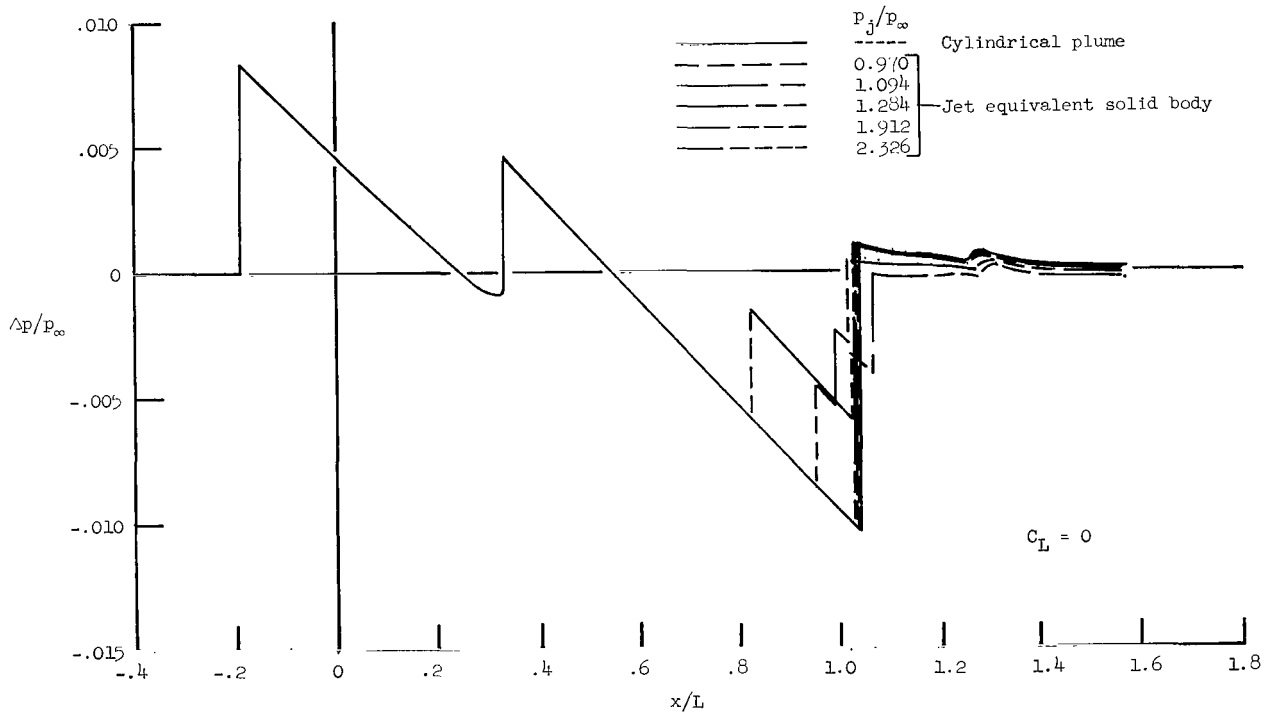
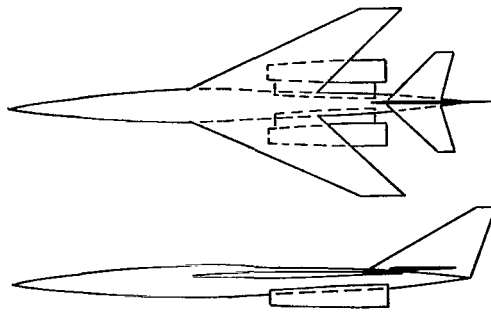


(f) Nozzle 6.



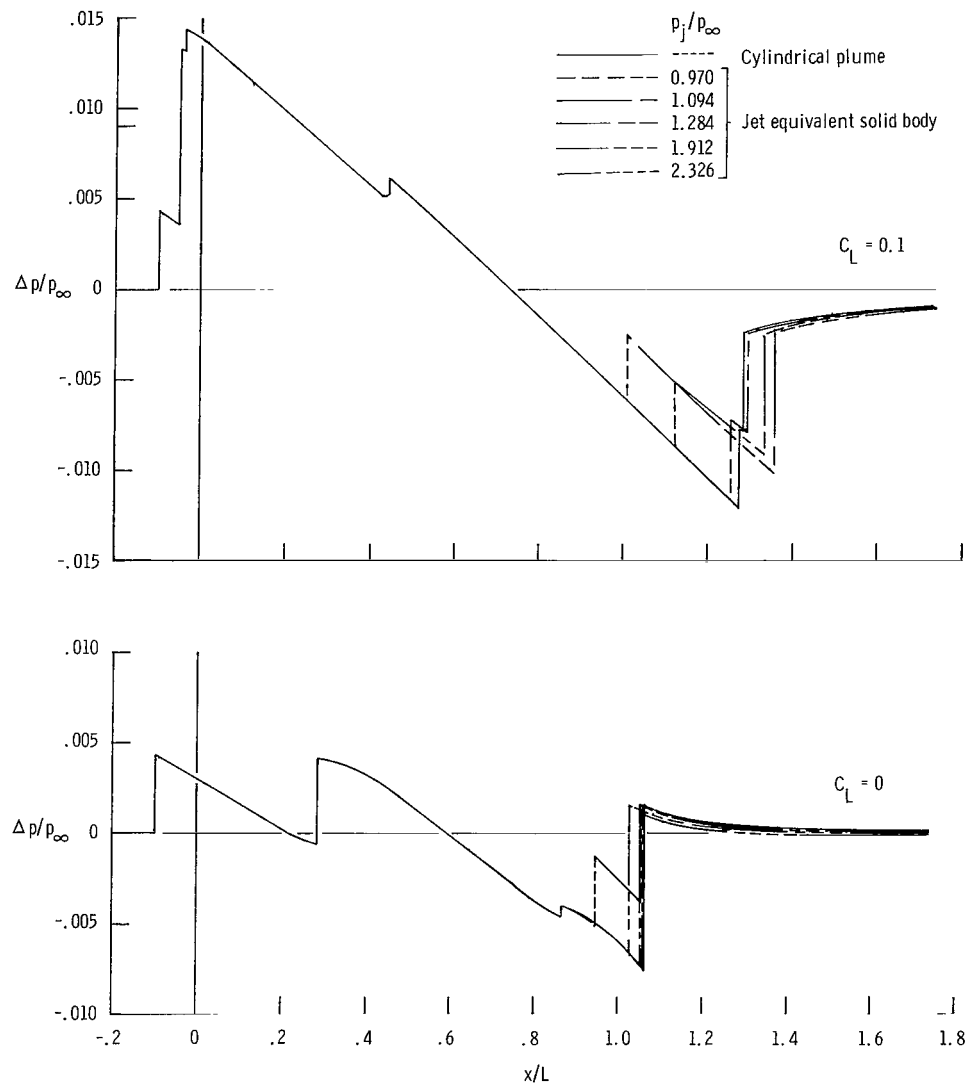
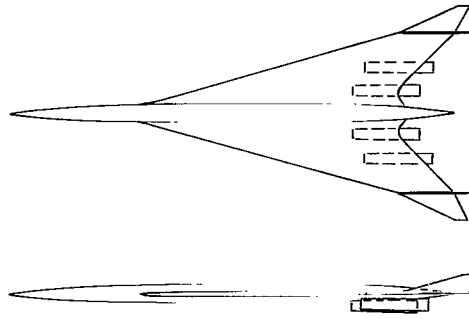
(g) Nozzle 7.

Figure 19.- Concluded.



(a) Fighter airplane with two podded engines.

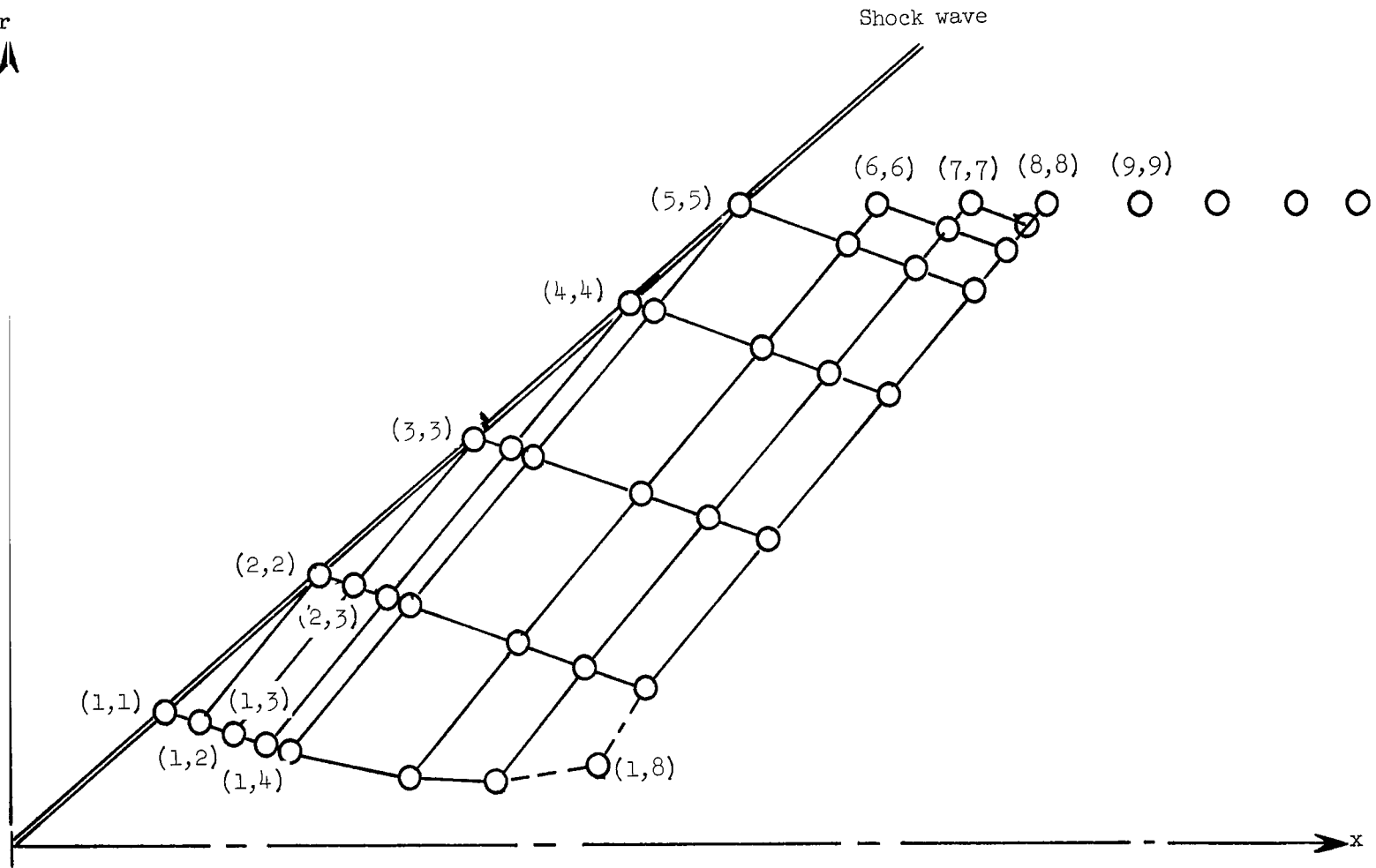
Figure 20.- Effect of jet plume on sonic-boom pressure signature of podded-engine fighter airplane and supersonic transport airplane with nozzle 4. $M_\infty \approx 2.20$.



(b) Supersonic transport airplane with four podded engines.

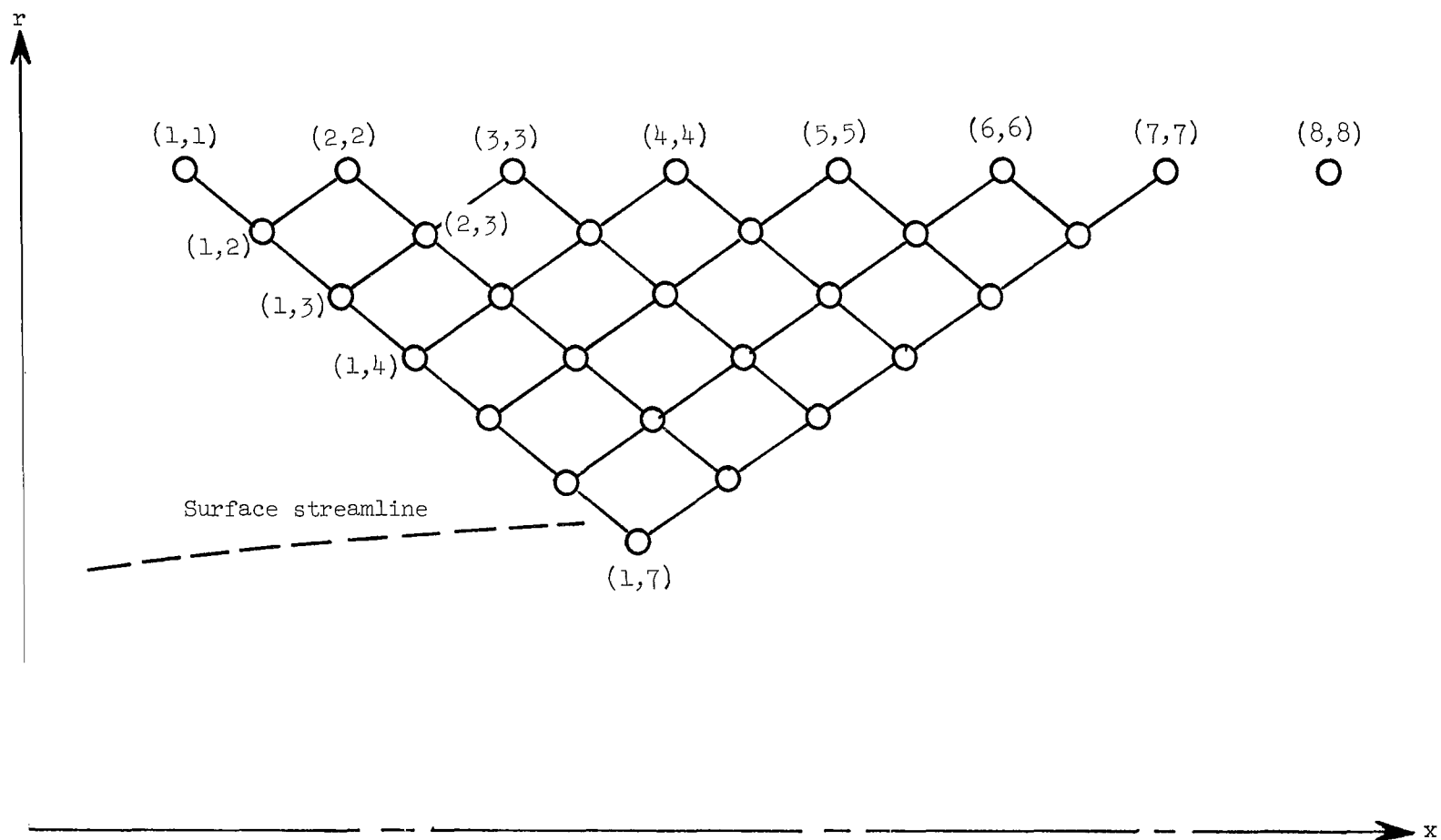
Figure 20.- Concluded.

r
↑



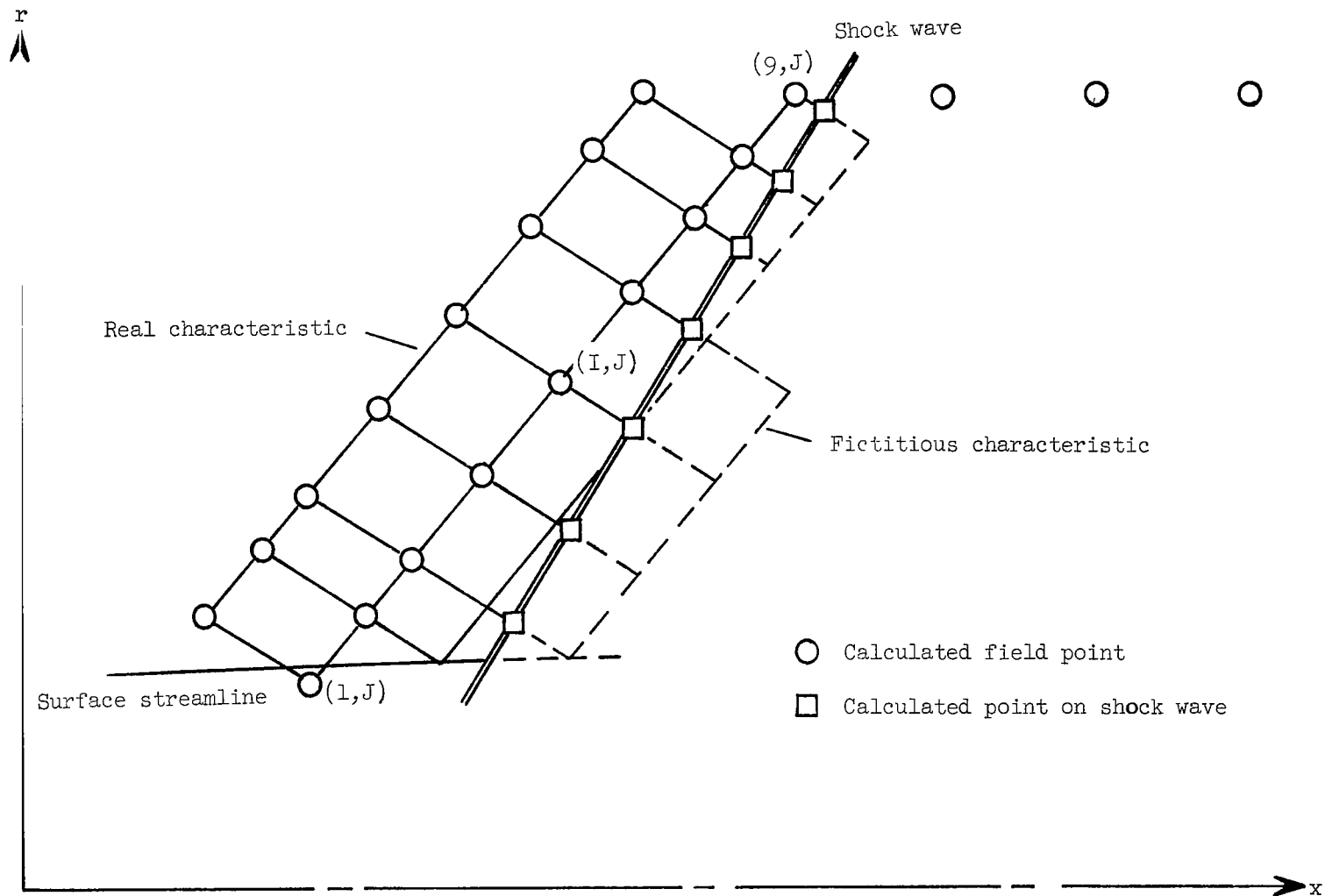
(a) Solution started just behind initial shock wave.

Figure 21.- Examples of characteristic-net calculations.



(b) Solution started in flow field.

Figure 21.- Continued.



(c) Solution in region of embedded shock wave.

Figure 21.- Concluded.

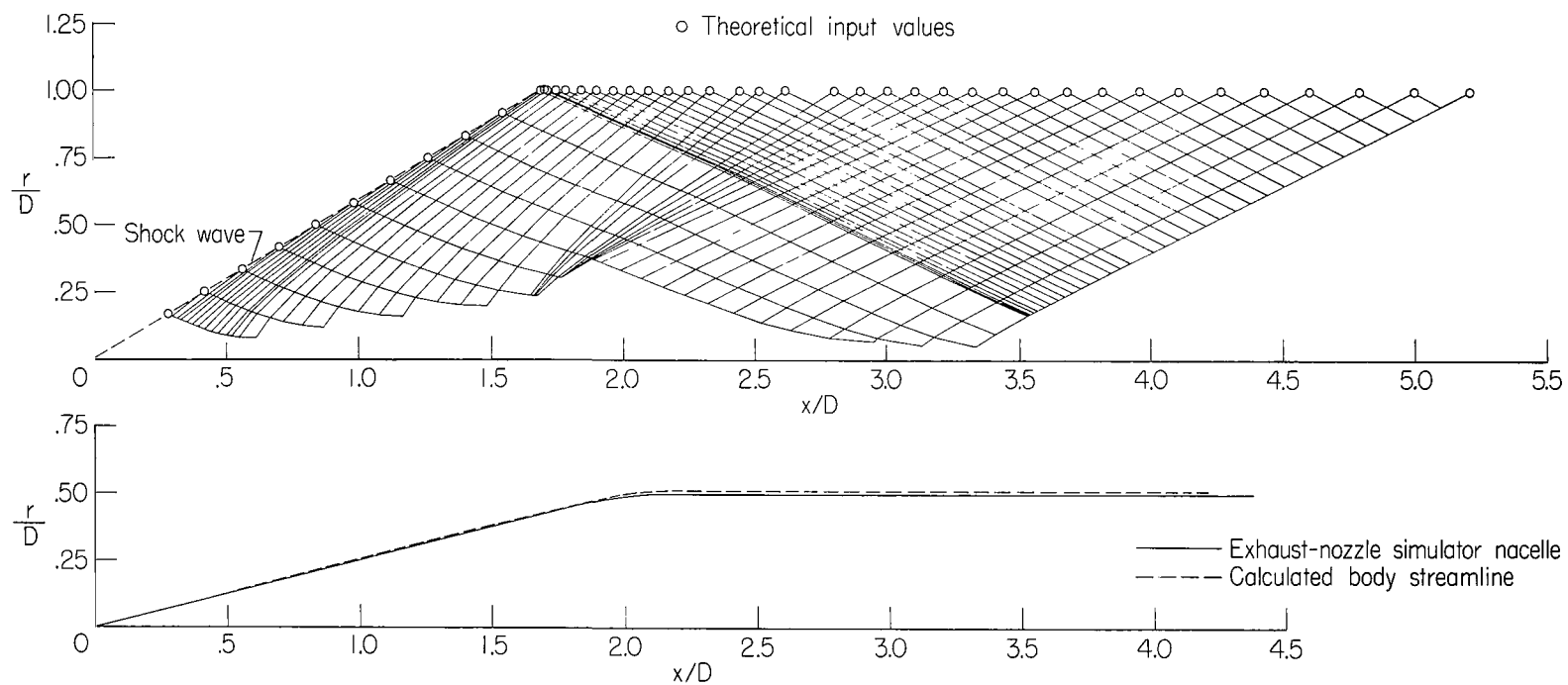


Figure 22.- Equivalent body shape and characteristic net for exhaust-nozzle simulator nacelle. Theoretical inputs to computer program. $M_\infty = 2.20$.
(Three iterations used to calculate characteristic net.)

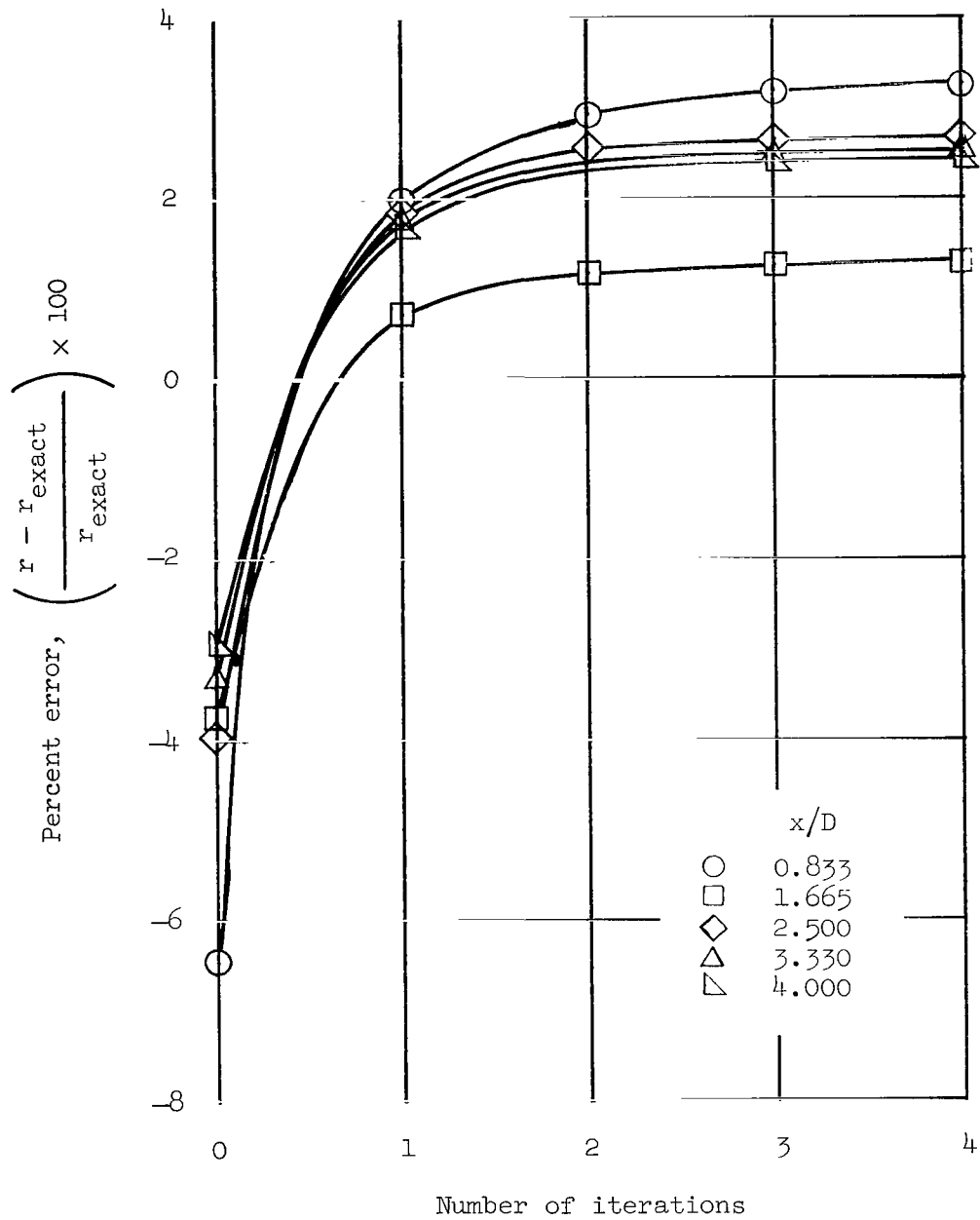


Figure 23.- Effect of number of iterations on error in calculating body streamline of jet-engine exhaust-nozzle simulator from theoretical flow-field quantities.

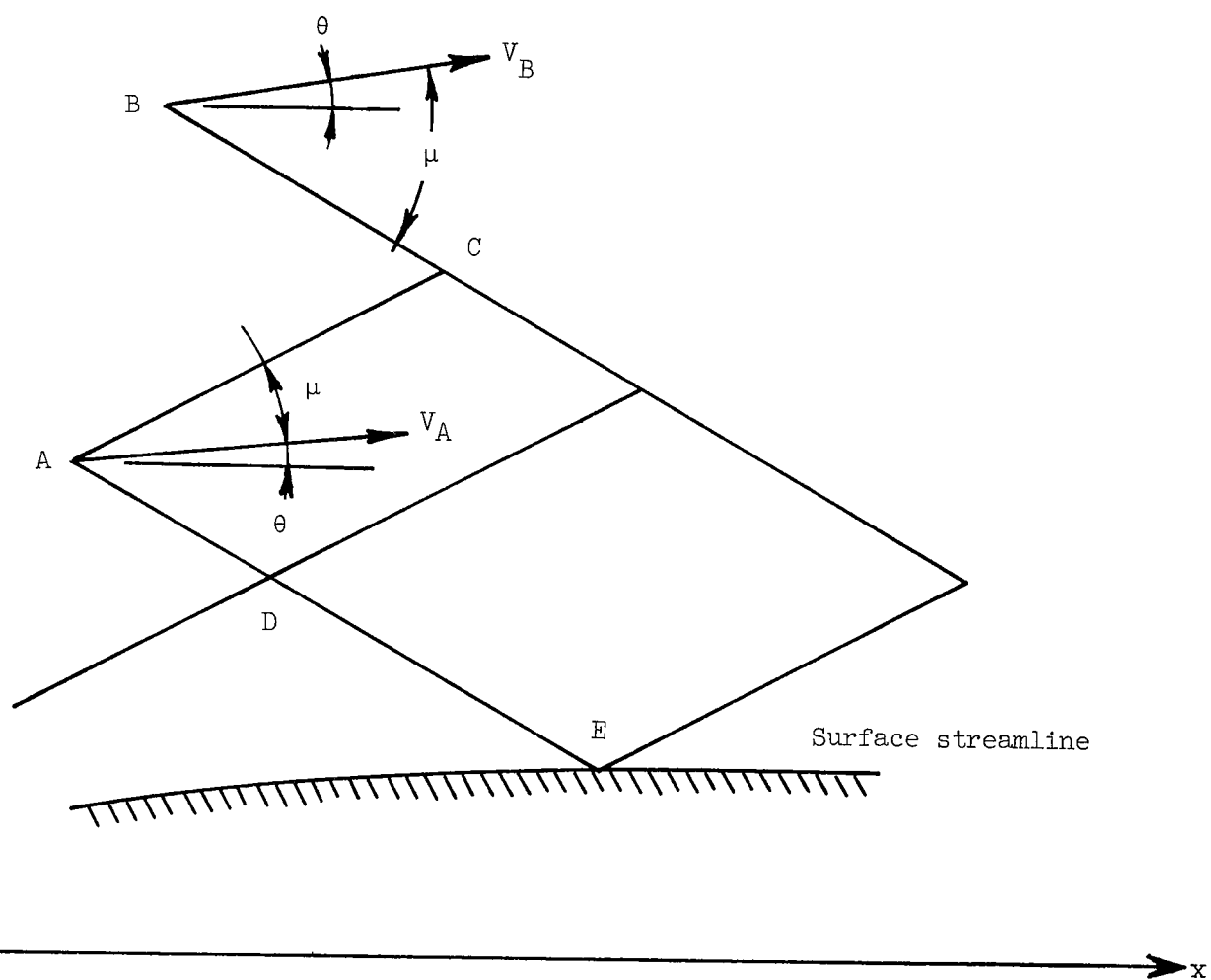


Figure 24.- Example of characteristic-net calculations.

NATIONAL AERONAUTICS AND SPACE ADMINISTRATION

WASHINGTON, D. C. 20546

OFFICIAL BUSINESS

FIRST CLASS MAIL



POSTAGE AND FEES PAID
NATIONAL AERONAUTICS AND
SPACE ADMINISTRATION

69328 00903
OZU 001 26 51 305
AIR FORCE WEAPONS LABORATORY/WLIL/
KIRTLAND AIR FORCE BASE, NEW MEXICO 8711

ALL L. LUD BOSTON, CHIEF, TECH. LIBRARY

POSTMASTER: If Undeliverable (Section 158
Postal Manual) Do Not Return

"The aeronautical and space activities of the United States shall be conducted so as to contribute . . . to the expansion of human knowledge of phenomena in the atmosphere and space. The Administration shall provide for the widest practicable and appropriate dissemination of information concerning its activities and the results thereof."

— NATIONAL AERONAUTICS AND SPACE ACT OF 1958

NASA SCIENTIFIC AND TECHNICAL PUBLICATIONS

TECHNICAL REPORTS: Scientific and technical information considered important, complete, and a lasting contribution to existing knowledge.

TECHNICAL NOTES: Information less broad in scope but nevertheless of importance as a contribution to existing knowledge.

TECHNICAL MEMORANDUMS:
Information receiving limited distribution because of preliminary data, security classification, or other reasons.

CONTRACTOR REPORTS: Scientific and technical information generated under a NASA contract or grant and considered an important contribution to existing knowledge.

TECHNICAL TRANSLATIONS: Information published in a foreign language considered to merit NASA distribution in English.

SPECIAL PUBLICATIONS: Information derived from or of value to NASA activities. Publications include conference proceedings, monographs, data compilations, handbooks, sourcebooks, and special bibliographies.

TECHNOLOGY UTILIZATION PUBLICATIONS: Information on technology used by NASA that may be of particular interest in commercial and other non-aerospace applications. Publications include Tech Briefs, Technology Utilization Reports and Notes, and Technology Surveys.

Details on the availability of these publications may be obtained from:

SCIENTIFIC AND TECHNICAL INFORMATION DIVISION
NATIONAL AERONAUTICS AND SPACE ADMINISTRATION
Washington, D.C. 20546